

Contents lists available at [ScienceDirect](https://www.sciencedirect.com)

# Case Studies in Construction Materials

journal homepage: [www.elsevier.com/locate/cscm](http://www.elsevier.com/locate/cscm)

## Determination of the mechanical properties and gamma-neutron shielding effectiveness of ultra-high performance dense concrete (UHPdC) exposed to high temperatures

Muhd Afiq Hizami Abdullah<sup>a,b</sup>, Raizal S.M. Rashid<sup>a</sup>, Abdullah Alnutayfat<sup>c,\*</sup>

<sup>a</sup> Department of Civil Engineering, Faculty of Engineering, Universiti Putra Malaysia, Serdang, Selangor 43400, Malaysia

<sup>b</sup> Department of Civil Engineering Technology, Faculty of Civil Eng. Tech., University Malaysia Perlis, Perlis 02100, Malaysia

<sup>c</sup> Department of Civil Engineering, College of Engineering, Prince Sattam Bin Abdulaziz University, Alkharj 11942, Saudi Arabia

### ARTICLE INFO

#### Keywords:

Gamma-rays

Neutrons

Heavyweight aggregates

High temperatures

Ultra-high-performance concrete (UHPC)

Radiation shielding

### ABSTRACT

Nuclear energy is integral in producing energy with net-zero emissions but widening its adoption requires advanced radiation shielding material. While concrete is widely used as radiation shielding material, there is a lack of study on shielding using ultra-high-performance concrete (UHPC) despite it being the most advanced concrete material to-date. This study delves into the mechanical properties and the shielding capabilities of denser UHPC (ultra-high-performance dense concrete, UHPdC) against both gamma-rays and neutron radiation, particularly under high-temperature scenarios. Three mixtures of UHPdC are composed of sand, barite, and magnetite, separately, with a common incorporation of colemanite, steel and polyvinyl alcohol (PVA) fibers. These mixtures are subjected to temperatures of 400 and 800 °C, assessing their microstructural changes via X-ray  $\mu$ -CT analysis, mechanical strength, and their gamma-rays and neutron shielding properties. Key findings revealed that sand UHPdC exhibited the highest compressive strength of 131.0 MPa, while magnetite UHPdC showed superior shielding against neutron radiation and gamma-rays emitted by Co-60, demonstrating enhanced effectiveness of more than 17 % and 12 %, respectively, compared to other types. The durability of magnetite UHPdC was notably robust up to 400°C, attributed to the thermal stability of its iron oxide content. However, at 800°C, all variants exhibited diminished shielding properties, likely due to degradation of neutron moderators and absorbers at the lower temperature. This research underscores the potential of UHPdC, especially magnetite-based, as a formidable material in nuclear infrastructure, capable of withstanding extreme conditions while providing effective radiation shielding. In addition, future studies should focus on the optimizing mix designs of UHPdC to mitigate the impacts of high temperatures, thereby enhancing the structural integrity and longevity of nuclear facilities.

### 1. Introduction

Nuclear power has been a cornerstone in the generation of electricity and in applications such as non-destructive imaging, essential for modern living [1]. A typical nuclear plant operates similarly to a thermal power station, but it uses a nuclear reactor to produce heat

\* Corresponding author.

E-mail address: [a.alnutayfat@psau.edu.sa](mailto:a.alnutayfat@psau.edu.sa) (A. Alnutayfat).

<https://doi.org/10.1016/j.cscm.2024.e04157>

Received 7 July 2024; Received in revised form 10 December 2024; Accepted 24 December 2024

Available online 4 January 2025

2214-5095/© 2024 The Author(s). Published by Elsevier Ltd. This is an open access article under the CC BY-NC-ND license (<http://creativecommons.org/licenses/by-nc-nd/4.0/>).

[2]. This heat is subsequently transformed into steam, which drives a steam turbine connected to a generator that produces electricity [3]. Nuclear energy is regarded as a clean energy source because it does not release carbon emissions, thus helping to decrease CO<sub>2</sub> levels [4]. Although there is a growing emphasis on renewable energy sources, nuclear energy continues to play a crucial role in global electricity production [5], supplying about 10 % of global electricity [6]. Currently, 30 nations have a total of 439 operational nuclear reactors, with another 64 planned or under construction [7]. Nuclear energy represents almost 10 % of the total global energy supply [8]. In Europe, for instance, nuclear energy is a major component of the electricity mix, providing over one-quarter of all electricity. It meets over 30 % of the region's energy needs, with fossil fuels and renewables providing the remainder [9]. As of 2024, Europe has 131 nuclear reactors in operation, with three additional reactors under construction in European Union countries [9]. By 2040, the nuclear energy agency has developed a detailed sustainable development strategy to decrease dependency on fossil fuels, including an anticipated 55 % increase in nuclear capacity [10].

The study of gamma radiation's influence on concrete deterioration has been challenging due to a lack of comprehensive empirical research [11]. Radiogenic heating, identified as a key consequence of gamma exposure on cement-based materials [12], adversely affects their mechanical integrity, mass, and dimensional stability, similarly to traditional heating methods [11]. Some research indicates that heavyweight aggregates like barite can diminish compressive strength, whereas magnetite might enhance it [13,14]. Furthermore, incorporating nano-ferrite into barite concrete has been shown to enhance its overall strength [17]. The addition of fine fillers has been found not only to increase the mechanical strength but also to improve the radiation shielding capabilities of concrete by incorporating neutron-absorbing elements [15]. Moreover, concrete with an optimal addition of colemanite has demonstrated improved compressive strength [16]. Studies have also noted enhanced neutron shielding in concrete with colemanite due to the integration of heavyweight aggregates and ferro-boron [17].

The importance of studying the microstructural changes in irradiated concrete cannot be overstated, especially for radiation shielding applications. Research has focused on incorporating elements that enhance concrete's protective properties [13,18–20]. The effectiveness of concrete as a shielding material depends on factors such as radiation intensity, material density, and the atomic numbers of the incorporated elements. Moreover, critical properties like mechanical durability, cost efficiency, and resistance to radiation-induced damage are essential [21,22].

While gamma radiation typically does not significantly affect the elastic modulus or the compressive, tensile, and flexural strengths of cement-based materials, it does influence other aspects [23,24]. For instance, studies indicate that concrete porosity decreases upon exposure to radiation [25], potentially improving its resistance to weathering processes involving mass transfer [26]. This reduction in porosity may result from the transformation of calcite into vaterite and aragonite during the carbonation process, influenced by gamma radiation [27,28]. Understanding these microstructural changes is crucial for optimizing the performance and durability of concrete used in radiation shielding, ensuring it meets the necessary protective standards.

Furthermore, it has been observed that irradiation leads to a finer pore structure in concrete, cutting porosity by approximately 50 %, which may improve its durability against processes like carbonation, leaching, sulphate attack, chloride penetration, alkali-silica reaction, and acid attack [25,26,29]. This enhanced durability is likely due to the lower permeability and diffusivity resulting from the reduced porosity [30]. Semiquantitative analyses have shown a decrease in Ca(OH)<sub>2</sub> levels and an increase in CaCO<sub>3</sub> concentrations under gamma irradiation, suggesting that radiation may accelerate the carbonation process [27]. However, gamma radiation is unlikely to significantly accelerate carbonation in extremely humid environments near 100 % humidity and might even slow it down in drier conditions around 50 % humidity. The radiation generally encourages the formation of the less dense vaterite and aragonite forms of CaCO<sub>3</sub> instead of calcite, which helps to explain the decreased porosity seen in irradiated concrete [12].

Past studies have shown that gamma irradiation in concrete can create structural imperfections in nano-SiO<sub>2</sub>, reducing its particle size [31]. This change enhances the reactivity and effectiveness of nano-SiO<sub>2</sub> as a concrete additive. Notably, incorporating just 1 % (by mass) of nano-SiO<sub>2</sub> exposed to 100 kGy of gamma radiation can more than double the compressive strength of concrete, consistent with findings from other research [30]. Gamma rays, known for their ionizing properties, are believed to break covalent bonds within cement hydrates, generating radicals [32]. These radicals may facilitate the cross-linking of calcium silicate hydrate chains, potentially making the concrete more brittle [33]. The use of silica nanoparticles to improve the mechanical and durability properties of concrete, especially under varying temperatures, has been extensively studied [34]. Gamma irradiation within the range of 10–150 kGy is thought to produce defects in the structure of nano-SiO<sub>2</sub>, similar to effects observed in silicon-containing aggregates [31]. Therefore, irradiating nano-SiO<sub>2</sub> is considered to enhance its reactivity and positively impact concrete properties [35].

Ultra-high-performance concrete (UHPC) subjected to neutron irradiation typically suffers degradation due to both neutron exposure and accompanying thermal effects. It is noted that the reduction in the concrete's elastic modulus can be linked to both neutron-related damage and thermal deterioration [36]. These two damaging mechanisms are thought to operate independently [37]. Yet, it has been observed that temperature may affect how irradiation-induced damage progresses within the concrete [38]. Consistent with previous studies, neutron energy utilized in these assessments is around 0.1 MeV [24]. Under such experimental settings, the internal surface temperature of the concrete is approximately 65 °C, while the external surface remains at about 20 °C. Fast neutrons mainly dissipate energy through elastic collisions with the nuclei of light elements and through inelastic scattering with the nuclei of heavier elements. The energy levels of the lowest excited states are much lower in heavy elements compared to light elements [39]. In practical scenarios, such as in concrete biological shields, the material often faces restrictive conditions that may lead to further mechanical damage. Remarkably, the proximity to the radiation source can exacerbate the increase in neutron flux over time, compounding the overall degradation of the concrete.

Utilization of UHPC as radiation shielding material is very significant as the importance of high mechanical strength in concrete is pivotal for ensuring durability, especially since traditional radiation shielding concrete often exhibits limited thermal resilience in terms of strength and protective capabilities [40]. UHPC, characterized by a compressive strength exceeding 200 MPa and a flexural

strength above 20 MPa, has been extensively researched [41–44]. Its ability to withstand high temperatures makes it particularly valuable for nuclear structures [45,46]. However, recent findings suggest that incorporating heavyweight aggregates and polyvinyl alcohol (PVA) fibers into UHPC may reduce its strength, despite their advantages for radiation shielding and heat resistance [47–50]. Currently, data on the gamma-neutron shielding effectiveness of UHPC when subjected to heat damage remains scarce. Moreover, the combined effects of neutron-absorbing elements like sand, magnetite, barite, colemanite and PVA fibers on UHPdC's performance as a radiation shielding material are not well-explored, prompting a need for further research. Consequently, this study focuses on evaluating the impact of heat on both the mechanical properties and the gamma-neutron shielding capabilities of UHPC. This involves integrating colemanite and reinforcing the mixture with PVA fibers to develop as innovative and sustainable form of concrete, termed ultra-high performance dense concrete (UHPdC).

## 2. Materials and methods

### 2.1. Materials

The components utilised in fabricating the specimens of ultra-high performance dense concrete (UHPdC) comprise of ordinary Portland cement (OPC), silica fume, fine aggregate, superplasticizer of polycarboxylic-ether based, and water. The OPC utilised in this investigation is classified as type 1 and is obtained from Tasek Corporation Berhad, adhering to the requirements specified in ASTM C150 [51] (Fig. 1). Three types of fine-sized primary materials, namely sand, barite, and magnetite, are utilised to manufacture three different types of UHPdC. Colemanite is incorporated into each form of UHPdC composition, substituting a portion of the primary aggregate, in varying percentages. The sand utilised in this investigation is obtained from a river and subsequently sifted into three distinct size categories: 0.65 – 300  $\mu\text{m}$ , 300–600  $\mu\text{m}$ , and 0.6 – 1.18 mm (Fig. 1a). The Minerals and Geoscience Department Malaysia provides barite, which is then crushed to a diameter of less than 1.18 mm (Fig. 1b). Magnetite is sourced from the steel ore mine of Bestagold Sdn. Bhd. in Sungai Petani, Kedah. The particle size of the magnetite is smaller than 1.18 mm, as shown in Fig. 1c. The particle of colemanite is in the form of powder and it is obtained from Turkey (Fig. 1f). Using fine-sized colemanite in ultra-high performance dense concrete (UHPdC) is crucial for optimizing its neutron shielding properties. The fine size of colemanite particles allows for a more uniform distribution throughout the concrete matrix, preventing the concentration of colemanite at specific points. In neutron shielding applications, any inhomogeneity can lead to areas of reduced shielding effectiveness, compromising the overall protective capability of the concrete. Fine-sized colemanite ensures that the neutron-absorbing properties are consistently maintained throughout the material, providing reliable and effective shielding. Moreover, the improved homogeneity contributes to the

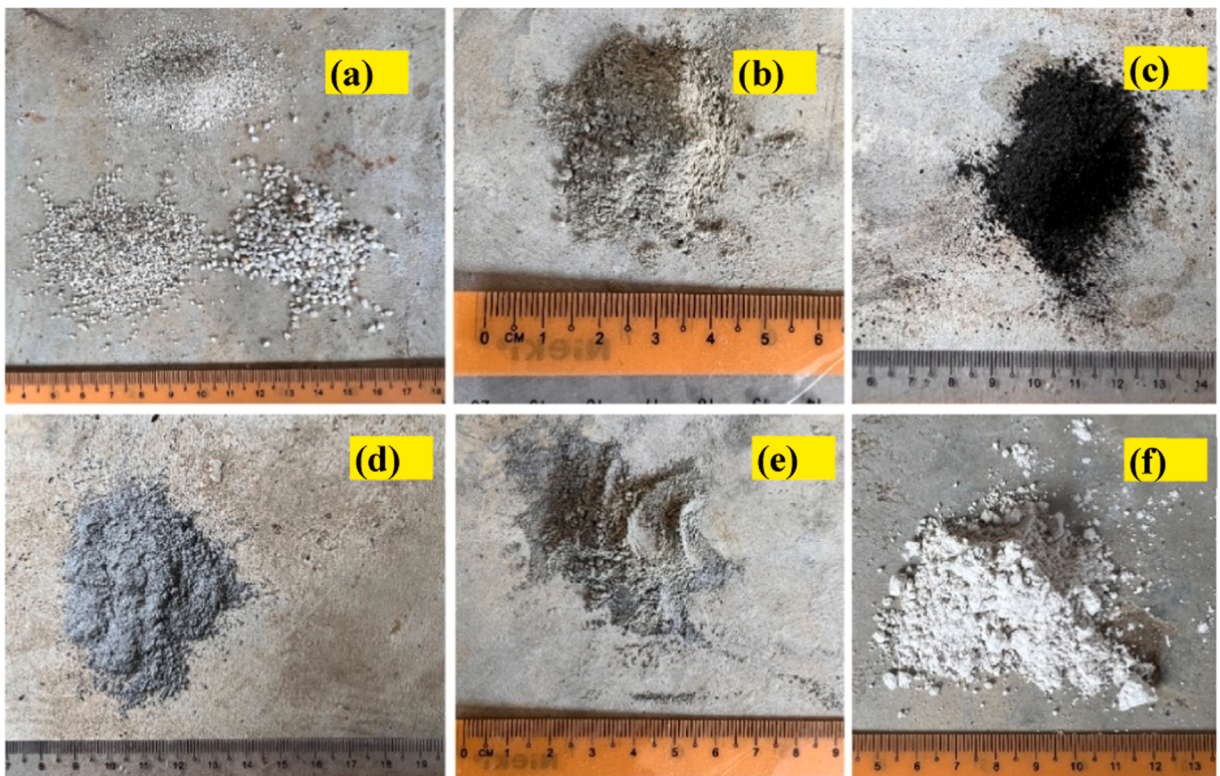


Fig. 1. Actual depiction size of (a) sand, (b) barite (c) magnetite, (d) silica fume, (e) cement, and (f) colemanite.

mechanical integrity of the UHPdC. By avoiding the formation of weak points, the concrete maintains its superior strength and durability, which are essential characteristics for both structural performance and long-term stability in radiation environments. Therefore, the use of fine-sized colemanite not only enhances the neutron shielding properties but also supports the overall performance and reliability of UHPdC in demanding applications. Table 1 displays the density of sand, magnetite, barite, and colemanite utilised in the investigation.

Fig. 2a,b displays the microstructure of sand and barite, with particle sizes ranging from 8.033 to 288.5  $\mu\text{m}$ . The barite particles are typically angular and predominantly fall within the size range of 40 – 66  $\mu\text{m}$ , as observed under a 4000  $\times$  magnifications (Fig. 2i-a,b,c). In the case of magnetite, the particles exhibit angular shapes, while there are also a significant number of particles that have a cylindrical shape. This phenomenon is evident at all levels of magnification, since the particles of magnetite exhibit a distinct elongation on one side. It is found that when it comes to particle size, magnetite is somewhat larger than barite. This is demonstrated at magnifications of 200  $\times$  and 1000  $\times$ , where the majority of particles fall within the size range of 37 – 339  $\mu\text{m}$ . At a 200  $\times$  magnification (Fig. 2ii-d,e,f), only a small number of particles smaller than 40  $\mu\text{m}$  can be seen, in contrast to the barite sample at the same magnification. The size of colemanite particles is smaller than that of barite and magnetite. This is seen at a magnification of 200  $\times$ , revealing a substantial region containing particles less than 25  $\mu\text{m}$  in size. The size of these particles is between 12 – 22  $\mu\text{m}$ , as observed at a magnification of 4000  $\times$ . Nevertheless, the particles have an angular structure, with just a small number of particles displaying a cylindrical form.

The steel fibres have been used as seen in Fig. 3. The fibre comes from Ganzhou Daye Metallic Fibres Co., Ltd. and is a straight steel fibre that is copper-coated and 20 mm long and 0.2 mm wide. This kind of steel fibre has a tensile strength of 2850 MPa and a density of 7840  $\text{kg/m}^3$ .

## 2.2. Mix composition

This study had produced three varieties of UHPdCs, namely sand UHPdC, barite UHPdC, and magnetite UHPdC. Each type of UHPdC contained 50  $\text{kg/m}^3$  of colemanite and 9.75  $\text{kg/m}^3$  of PVA fibre, as indicated in Table 2.

## 2.3. Methods

### 2.3.1. Preparation of specimens

The preparation of samples for the study involves three steps: mixing, flow table testing, and heat curing. Three types of fine aggregates were prepared for each UHPC mixture as per Table 2. A 300 kg capacity mixer was used to dry mix cement and silica fume at low speed for 2 minutes. Fine aggregates were then blended for 6 minutes. Next, 50 % of the super-plasticizer of polycarboxylic ether type, pre-mixed with 70 % water was added and mixed at medium speed for 3 minutes. The remaining super-plasticizer and water were added as the mixture's workability increased. Mixing continued for 1 minute before assessing workability using a flow table test. The fresh UHPC mix was compacted using a vibrating table. This process results in a total of 36 cubic samples, measuring 100  $\times$  100  $\times$  100 mm and 12 prism samples measuring 100  $\times$  100  $\times$  500 mm (Fig. 4a, b and c). Three cubic samples were produced for each type of UHPdC, however only one prism was produced for each UHPdC (Fig. 4d). Cubic samples were employed in the ultrasonic pulse velocity (UPV) test and compressive strength test, whilst prism samples were sliced to a thickness of 20 mm for observation under a stereomicroscope and testing for gamma ray and neutron shielding (Fig. 5).

The workability of the mixes was also assessed using flow table equipment, following the guidelines of EN 12350-5 [50]. This is accomplished by employing a manual flow table instrument to test the consistency of the fresh mix prior to pouring it into moulds. The flow table is equipped with a central top disc on which a mixture of UHPdC is poured into a mould. The sample is positioned between two layers, and any surplus material is removed by carefully scraping it off with a palette knife. After filling the mould with the sample, the mould is taken out and the disc is vigorously shaken 15 times at a consistent rate of 1 shake per second using a side lever. The spread-out sample is measured with precision to the nearest millimeter.

The UPV test was conducted in accordance with the BS EN 12504-4 [52] and the transducers are directly aligned to measure the pulse velocity. The samples were tested for compressive strength at 28 days of concrete age. Prior to commencing the testing, lubricants are applied to the surface of both transducers. Transducers are positioned on opposing surfaces, creating a configuration known as direct transmission. Three measurements of ultrasonic wave velocity are taken for each sample. Subsequently, the samples undergo testing to determine their compressive strength.

For stereomicroscope analysis, prism sample of 20  $\times$  100  $\times$  100 mm is analysed for pores distribution located the center of the prism within the area of 5  $\times$  5 mm. Pores are counted and measured for diameter using the stereomicroscope. The compressive strength test is performed following the guidelines of BS EN 12390-3 [53], with a loading rate of 80 MPa/min (Fig. 6a, b). Cubic

**Table 1**  
Physical properties of aggregates.

Type of aggregate	Particle size, mm	Density, $\text{kg/m}^3$
Sand	0.30–1.18	2700
Magnetite	0.065–0.60	4140
Barite	0.065–0.60	4013
Colemanite	< 0.3	2400

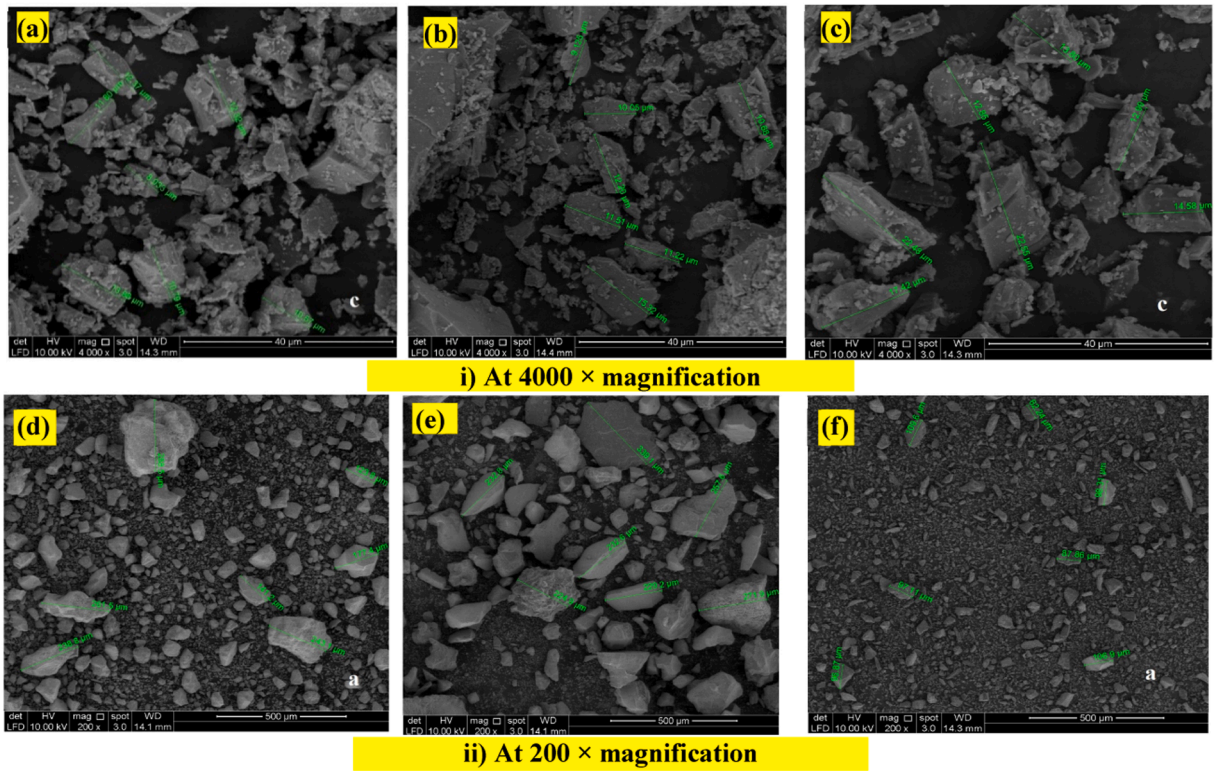


Fig. 2. SEM analysis of (a) barite, (b) magnetite, and (c) colemanite at 4000 and 200 × magnifications.

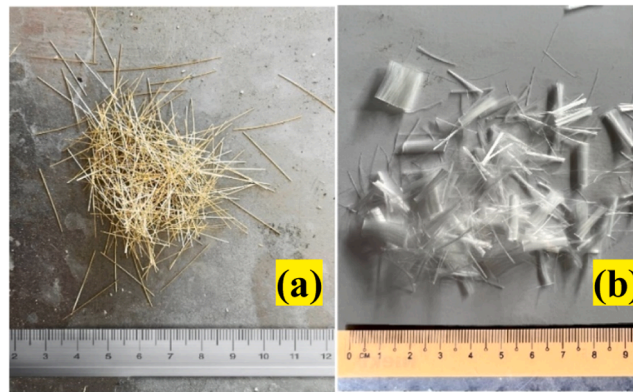


Fig. 3. An actual depiction of (a) steel fibres and (b) PVA fibre.

Table 2  
Mixture design for UHPdC.

Sample	Cement	Silica Fume	Sand	Magnetite	Barite	Colemanite	Super plasticizer	Steel fibres	PVA fibres	Water
USS95C5	825	200	950	-	-	50	28	120	9.75	183
UM95C5	825	200	-	1865	-	50	33	120	9.75	223
UB95C5	825	200	-	-	1580	50	33	120	9.75	223

specimens are subjected to testing after a concrete age of 28 days. The sample is thoroughly cleaned and flattened before being positioned at the center of the hydraulic press. The sample is subjected to a steady rate of 80 MPa/min until it can no longer support a higher stress. To observe the pores, sections of the prism sample are examined under a stereomicroscope, focusing on a 100 mm<sup>2</sup> area

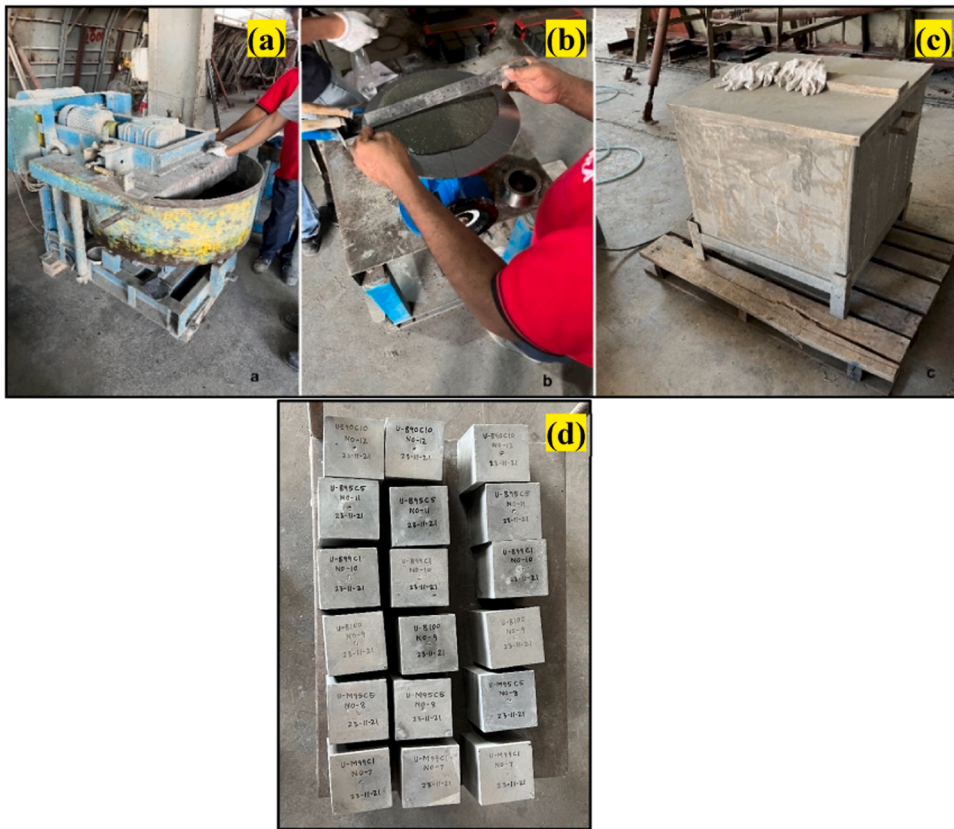


Fig. 4. Processes involved in producing the samples which include (a) mixing process, (b) flow table test, (c) heat curing process, and (d) prepared cube samples for compression test.

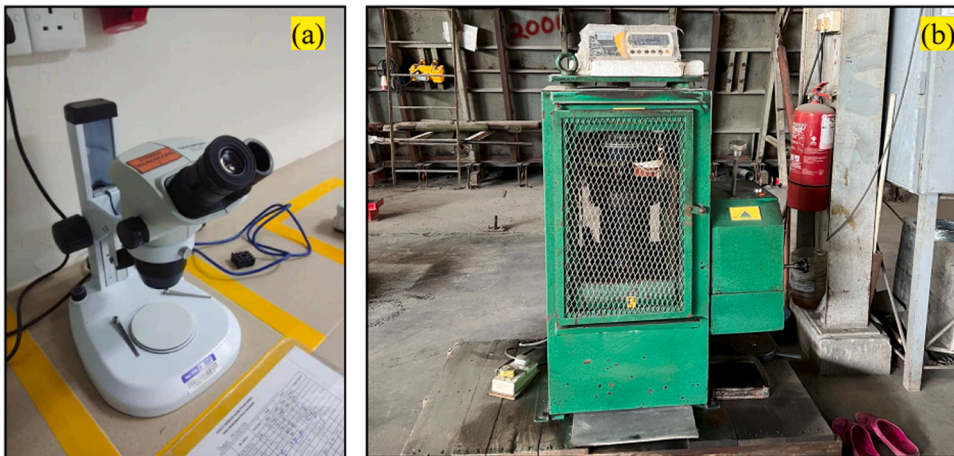


Fig. 5. (a) Stereomicroscope, and (b) compression strength test machine that is setup in accordance to BS 12390-3 [49].

located near the center of the sections. For each variety of UHPdC, a total of 6 slices are examined. Prior to initiating the observation, the surface of the sample is thoroughly cleansed and cleared of any extraneous matter. The image obtained from the observation is examined to determine the dimensions and quantity of pores observed inside the designated region.

Regarding radiation shielding qualities, two types of radiation tests were conducted: gamma ray and neutron shielding tests. The specimens were obtained by cutting prism-shaped samples into slices with a thickness of 20 mm using a concrete cutter (Fig. 6a). The slice samples are subjected to air-drying prior to being tested for radiation shielding, as shown in Fig. 6b. Fig. 7a illustrates the spatial separation between the radiation source, sample, and detector. This equipment setup is utilized for testing both gamma ray and

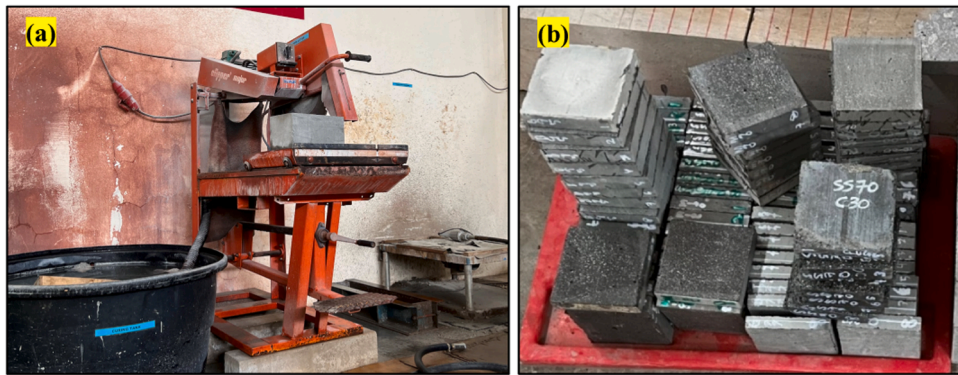


Fig. 6. Depiction of concrete (a) cutter and (b) Slice samples.

neutron sources. The radiation source in the experimental setup is meticulously shielded to ensure safety. The source is housed within a fully enclosed lead container, with a slit opening that is less than 8 mm wide. This narrow slit restricts the passage of radiation, allowing radiation to pass through in a single plane, directed towards the front. To further enhance safety, lead blocks are strategically placed on the sides and back of the setup. This configuration effectively contains radiation, providing robust protection for users and minimizing exposure risks.

The distances between the detector, test sample, and radioactive source range from 2 to 40 cm. The design in this investigation replicates the configuration employed for the UHPC sample. The radiation sources utilised for gamma-ray shielding are Cs-137 (2 mCi) and Co-60 (1.14 mCi), which are detected using a NaI scintillating detector. The detector, which is attached to the counter, detects penetrating radiation. Counting is conducted for duration of 6 seconds for every layer of the sample, and 3 measurements are recorded for each observation.

In this study, the high activity of the gamma source necessitates a short counting duration of 6 seconds to prevent the data logger from being overwhelmed. Despite this brief observation period, the precision of the results remains unaffected. The high activity ensures a substantial number of counts even within a short time frame, which enhances statistical accuracy. Moreover, the shorter duration prevents data saturation, ensuring that the data logger accurately records the number of penetrated gamma rays. The high number of counts recorded through the full thickness of concrete allows for a precise assessment of its shielding properties. By effectively managing the counting duration, the study achieves reliable and precise measurements of the radiation shielding capabilities of concrete.

The source utilised for neutron shielding was AmBe with an activity of 23.88 mCi, which was observed by a Helium-3 neutron detector (Fig. 7b). The penetration count is conducted for duration of 60 seconds, with three measurements recorded for each section of the sample. The 60-second radiation penetration for the neutron source compared to 6 seconds for the gamma source is due to the different properties of these radiations. Gamma rays, being high-energy electromagnetic waves, penetrate materials more efficiently than neutrons, which are particles with mass. Neutrons interact with atomic nuclei, leading to more absorption and scattering, thus requiring longer exposure. Furthermore, the activity levels of the sources differ, affecting the intensity and duration needed for penetration. Eight samples were examined for each type of UHPdC in every shielding test.

The value of gamma ray shielding is determined by Lambert's Law, as expressed in Eq. (1). The linear attenuation coefficient ( $\mu$ ) can be calculated from the photon count value ( $D$ ) after passing through a sample with a specified thickness ( $t$ ), and the photon count value without the sample  $D_0$ . The value of  $\mu$  is calculated by determining the slope of the graph obtained by plotting the natural logarithm of the ratio  $\ln \frac{D_0}{D}$  versus time  $t$  [47]. Eq. (2) is used to compute the Tenth Value Layer (TVL), which is the ideal thickness for shielding 90 %

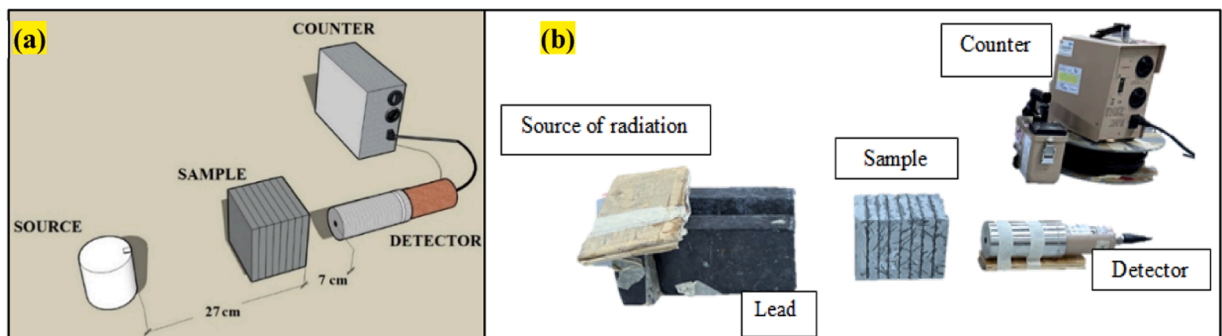


Fig. 7. (a) Schematic of test setup showing position and distance of source, sample, detector and counter, (b) actual test setup for gamma ray shielding.

of gamma rays, based on the value of  $\mu$ . In the context of neutron shielding, the calculation of the Macroscopic Removal Cross section or neutron shielding coefficient,  $\sum_R(E_n)$ , is determined using Eq. (2). In this equation, the value of  $\mu$  is replaced by  $\sum_R(E_n)$ , and it is computed based on the recorded counts obtained from exposure to an AmBe source. The TVL value for neutron radiation is determined by substituting the value of  $\mu$  with the summation of  $\sum_R(E_n)$  in Eq. (2).

$$D = D_0 e^{\mu t} \quad (1)$$

$$TVL = \frac{\ln 10}{\mu} \quad (2)$$

### 2.3.2. Heat exposure

To evaluate their durability, heat is applied to the samples. They are exposed to temperatures of 400°C and 800°C before undergoing tests for mechanical and shielding properties. The temperatures of 400°C and 800°C were chosen for this study based on previous research findings. Past studies have shown that heating UHPdC to 400°C results in an improvement in strength, while heating it to 800°C leads to a significant deterioration in strength [54]. By selecting these specific temperatures, this study aims to investigate the underlying mechanisms and effects of thermal exposure on a new mixture of UHPdC, providing a comprehensive understanding of its behavior under these critical conditions. An electric furnace is used to heat the samples, which are placed in a steel enclosure to protect the heating element from potential damage due to explosive spalling (Fig. 8a, b). The heating process involves raising the temperature at a rate of 5 °C/min and maintaining the target temperature for one hour. After the furnace cools to a safe handling temperature, the samples are removed.

### 2.3.3. X-ray computed tomography (CT) scan

For the X-ray  $\mu$ -CT analysis, small fractions of UHPdC samples containing optimized sand, barite, and magnetite were selected to study the microstructural effects of exposure to 800 °C (Fig. 9). The device used to capture 3D microstructural images was an X-ray micro-CT scanner equipped with an 11-megapixel resolution. Due to limitations in the sample holder size and X-ray penetration, the diameter of the UHPdC samples was restricted to less than 5 mm. The scanner featured an X-ray tube with adjustable settings ranging from 20 to 100 kV and power up to 10 W, and included a 12-bit cooled charge-coupled device camera connected to a scintillator.

To document the microstructural changes, the raw projection data were captured using the distortion-corrected 11-megapixel X-ray camera. The data collection specifically targeted the interface between the cement mortar overlay and the underlying concrete substrate. To minimize experimental time, exposure times were kept as brief as feasible, typically resulting in each scanning session lasting between 110 and 120 minutes. This duration was deemed suitable for assessing changes in microporosity at the interface. Initial tests conducted immediately after sample preparations were not satisfactory due to rapid microstructural changes that outpaced the scanning capability. Reducing both exposure times and the number of projections was considered to shorten overall scan duration; however, this adjustment could potentially increase artifacts and diminish image contrast. Thus, scanning parameters were carefully selected to balance the reduction of scan times with the maintenance of high-quality imagery. Moreover, the brief scanning periods helped reduce thermal stress on the samples, avoiding excessive water evaporation and preserving the integrity of the fresh paste. Moreover, it was also crucial to maintain consistent scanning and reconstruction parameters for sequential analyses of the same specimen at different stages. This consistency is a key in understanding how various UHPdC compositions withstand high temperatures, an essential factor for applications requiring excellent thermal resistance. Accuracy in each phase of the process is critical to ensure the reliability of data reflecting the microstructural properties of the heat-treated UHPdC samples.

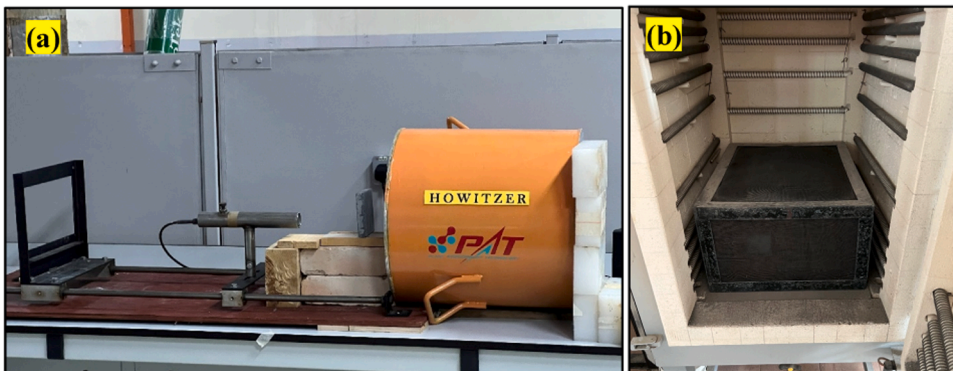


Fig. 8. Actual test setup for: (a) neutron shielding and (b) Furnace for heating the sample.

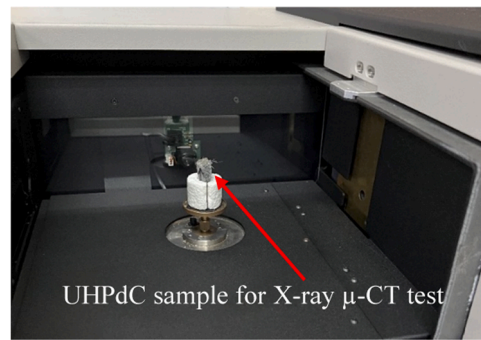


Fig. 9. An X-ray  $\mu$ -CT test setup for a UHPdC sample.

### 3. Results and discussions

#### 3.1. Properties of UHPdC

Table 3 presents the results of the properties of UHPdC samples. It can be seen that barite UHPdC exhibits the highest workability at 285 mm, which is approximately 67.6 % higher than sand UHPdC's 170 mm and 32.6 % higher than magnetite UHPdC's 215 mm, suggesting better ease of handling and pouring. Conversely, magnetite UHPdC is the densest with a density of 2991 kg/m<sup>3</sup>, marking an 8.4 % increase over barite UHPdC and a substantial 26 % increase over sand UHPdC. sand UHPdC, however, achieves the highest UPV at 4640 mm/s, which is 13.5 % and 5.7 % higher than barite UHPdC and magnetite UHPdC, respectively, indicating superior internal cohesion and material integrity. There is an inverse proportionality between the value of UPV and the density of UHPdC. The UPV value indicates the compactness of the matrix within the microstructure of UHPdC. Besides, the density of the produced UHPdC depends on the materials used, exhibiting that compactness is directly proportional to density". Magnetite and barite are significantly heavier and denser in terms of specific gravity compared to sand, leading to the production of denser concrete. However, the wider size gradation of sand particles results in a more compact matrix than that of magnetite and barite UHPdC. This is depicted by the SEM images of magnetite and barite which show particle sizes are less than 0.35 mm. Despite this, sand is lighter and less dense than barite and magnetite, resulting in a lower overall density.

It is also revealed that sand UHPdC is the leader in compressive strength at 131.0 MPa, which is 12.9 % and 10.3 % greater than magnetite UHPdC and barite UHPdC, respectively. Similarly, sand UHPdC outperforms in flexural strength with 20.048 MPa, about 37.5 % and 14.7 % higher than magnetite UHPdC and barite UHPdC, respectively. This is reflected in splitting tensile strength at 17.6 MPa, showing a 13.77 % and 18.05 % improvement over magnetite UHPdC and barite UHPdC, which is crucial for applications where resistance to tensile stressed is required. Superior performance of sand UHPdC in comparison to other sample is due to wider range of particle size distribution which resulted in denser and compactness of the concrete matrix [55]. Another study also shows lower splitting tensile strength of magnetite UHPdC in comparison to sand UHPdC [56]. This is due to different physico-mechanical characteristics of sand and magnetite. Furthermore, reduction in mechanical properties is also contributed by the weaker interfacial-transition zone of UHPC with higher water-to-cement content [57]. In the case of UHPC, however, compactness is crucial for mechanical strength, as the mix uses fine aggregates. There are no coarse aggregates in the mixes to contribute their strength to the concrete

In term of neutron shielding magnetite UHPdC possesses superior capability in neutron shielding, with 17.6 % higher effectiveness (0.0307 cm<sup>-1</sup>) than barite UHPdC and 17.2 % higher than sand UHPdC. For gamma ray shielding against Co-60, magnetite UHPdC also leads with a shielding measure of 0.1390 cm<sup>-1</sup>, 22.5 % and 12.1 % more effective than barite UHPdC and sand UHPdC, respectively. This is largely contributed by high density of magnetite aggregate compared to barite and sand. In general, these differences emphasize the unique applications for each UHPdC type, varying from general construction requiring high-strength and durability to specialized uses in radiologically protective environments as the radiation shielding effectiveness is directly proportional to the density of UHPdC.

Table 3

Properties of UHPdC samples.

Type of UHPdCs	Workability, mm	Density, kg/m <sup>3</sup>	UPV, mm/s	Compressive strength, MPa	Flexural strength, MPa	Splitting tensile strength, MPa	Gamma ray shielding, cm <sup>-1</sup> (Cs-137)	Gamma ray shielding, cm <sup>-1</sup> (Co-60)	Neutron shielding, cm <sup>-1</sup>
Sand UHPdC	170	2374	4640	131.0	20.048	17.553	0.1663	0.1156	0.0262
Barite UHPdC	285	2776	4083	116.0	14.047	14.385	0.1953	0.1306	0.027
Magnetite UHPdC	215	2991	4348	118.7	17.005	15.177	0.1972	0.1390	0.0307

### 3.1.1. Residual compressive strength

The residual compressive strength is measured by evaluating the compressive strength of samples that have been exposed to heating at 400°C and 800°C. It was observed that higher temperatures resulted in a reduction in compressive strength. When subjected to 400°C, sand and barite UHPdC showed a decrease in compressive strength by 19.4 % (116 MPa) and 8.8 % (105.6 MPa), respectively (Fig. 10). It is revealed that prolonging heat exposure could significantly further reduce the strength. However, magnetite UHPdC displayed consistent durability at temperatures up to 400°C, suggesting its thermal stability due to its Fe<sub>3</sub>O<sub>4</sub> composition, which maintains phase stability below 570°C [58]. The expansion of sand and barite caused cracks in the cured cement paste around the aggregate, leading to a decrease in compressive strength [59]. Barite aggregate has nearly twice the thermal expansion coefficient of magnetite, and sand undergoes a quartzite phase transition above 570°C [60,61]. At 400°C, sand UHPdC showed a larger decrease in compressive strength compared to other UHPdC samples. The low thermal resistance of sand UHPdC at 400 °C can be attributed to its increased heat capacity and thermal conductivity compared to denser aggregate [62].

The reduction in compressive strength is primarily due to the breakdown of cement hydration products. When concrete is subjected to heat, moisture gradually evaporates, initially enhancing hydration and thereby increasing early compressive strength [63]. This phenomenon can boost compressive strength by up to 10 % in certain mixtures at temperatures around 22°C [56]. Moreover, exposing concrete to temperatures up to 250°C has been shown to increase compressive strength by 8 %–15 % compared to unheated samples [64]. However, at higher temperatures, such as 500°C and 750°C, concrete experiences significant strength degradation, with reductions of approximately 12 % and 68 %, respectively, compared to samples maintained at ambient temperature [56]. This degradation occurs because temperatures above 250°C cause the evaporation of water within the cement matrix, leading to the decomposition of compounds such as C–S–H and C–S–A–H, which weakens their binding properties [65]. Moreover, when concrete is subjected to 800 °C, it experiences a dramatic 70 % reduction in compressive strength compared to unheated samples [66]. When temperatures exceed 500°C, the residual compressive strength of concrete can decrease by 33 %–48 %. This reduction is attributed to the volumetric expansion of both aggregates and fibers, the drying and decomposition of C–S–A–H gels, and the shrinkage resulting from the transformation of Ca(OH)<sub>2</sub> to CaO [67].

### 3.1.2. Residual flexural strength

It is exhibited that exposure to 400°C resulted in reduced flexural strength in UHPdC. sand had the highest residual flexural strength, measuring 14.8 MPa, which represents a 26.4 % loss (Fig. 11). The decrease in flexural strength is mainly attributed to the decomposition of cement hydration products that occur in all samples of UHPdC. This is followed by magnetite and barite UHPdC, which both measured 12.3 MPa with varying percentages of flexural strength loss. The reduction in flexural strength of UHPdC resulting from thermal exposure is primarily caused by the expansion of the aggregate, leading to internal cracking and consequently reducing the contact between the aggregate and steel fibers.

Moreover, the elevated temperature of 800°C caused the degradation of the steel fibers, further decreasing the flexural strength of UHPdC. Fig. 12 illustrates the alteration in color of steel fibers within sand, barite, and magnetite UHPdC. The black appearance of the steel fibers is a result of extensive oxidation, which is also evident when studying the morphologies of steel fibers at high temperatures [68]. According to the study, steel fibre experiences a loss of its structural integrity at this temperature because of cracking and peeling caused by the oxidation process. Consequently, the diminished reinforcing impact of steel fibre led to a decrease in the flexural strength of UHPdC. Besides, the copper coating of the steel fibre experienced oxidation when exposed to a temperature of 400 °C. This oxidation accounts for the relatively smaller reduction in flexural strength compared to exposure at 800°C. The decrease in flexural strength of UHPdC is primarily due to the expansion of steel fibers, which induces cracking and weakens the bond between the fibers and the cement paste within the aggregate [69].

It is found that when subjected to a temperature of 400 °C, sand UHPdC exhibited greater thermal resistance compared to the sand UHPdC exposed to 800 °C, as indicated by the residual flexural strength (Fig. 11). The transition of quartzite crystal occurs exclusively at temperatures above 570 °C, leading to significant breaking and an increase in volume [60,70]. The formation of fractures and the

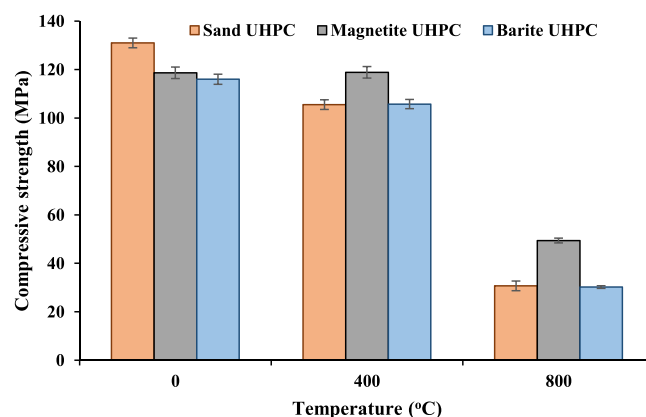


Fig. 10. Effect of temperature on compressive strength of optimised sand, barite and magnetite UHPdC.

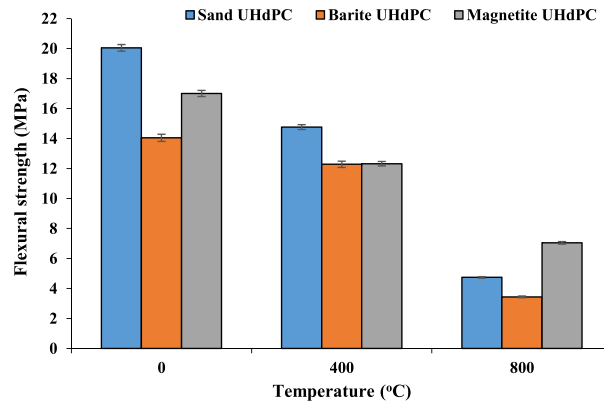


Fig. 11. Effect of temperature on flexural strength of optimised sand, barite and magnetite UHPdC.

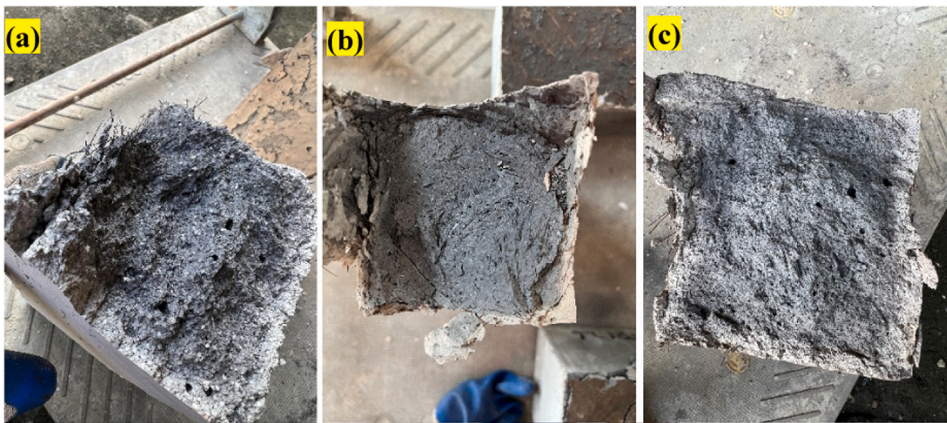


Fig. 12. UHPdC samples heated to 800 °C: (a) sand, (b) barite and (c) magnetite.

increase in void spaces within the sand UHPdC resulted in a decline in structural integrity and a reduction in the frictional interaction between the steel fibers and the aggregate, leading to a decrease in overall flexural strength. In contrast, barite UHPdC demonstrated superior thermal resistance at 400°C compared to sand UHPdC, as evidenced by the lower percentage reduction in flexural strength. This enhanced thermal resistance can be attributed to the higher density of barite, which contributes to its improved performance at elevated temperatures [62]. According to the study [62] that indicates the density of concrete significantly influences its thermal resistance. The research highlights that magnetite concrete, due to its higher density compared to quartz concrete, exhibits lower thermal conductivity and capacity. These properties are indicative of enhanced thermal resistance. Additional details have been included in the paragraph to enhance clarity.

However, subjecting barite to a temperature of 800 °C led to a significant decrease in flexural strength compared to exposure at 400°C. The expansion of barite caused the hardened cement paste to crack, resulting in inadequate contact with steel fibers and an overall decrease in flexural capacity. Magnetite UHPdC exhibits superior heat resilience up to 800 °C, as evidenced by its higher percentage of flexural strength retention. Moreover, it is reported that as temperatures increase, the reduction in tensile strength is more pronounced than in compressive strength [69]. Tensile strength is more significantly affected by the coalescence of cracks compared to compressive strength [71]. The formation and expansion of new cracks diminish the load-bearing capacity, intensifying the stress concentration at the tips of critical cracks [72]. Moreover, while compressive forces tend to close cracks, tensile forces cause them to widen.

Magnetite showed the highest residual flexural strength of 7.0 MPa after being exposed to 800°C. This represents a decrease of 58.6 % compared to the unheated sample (Fig. 11). Subsequently, the residual flexural strengths of barite and sand UHPdCs were measured at 3.4 MPa and 4.7 MPa, respectively. The strength decrease for sand and barite UHPdC was larger than that for magnetite UHPdC, at 76.3 % and 75.5 %, respectively. In general, the decline in flexural strength of UHPdC due to thermal exposure is primarily caused by the expansion of the aggregate, which induced internal cracking and diminished contact with the steel fibers. Moreover, exposure to the high temperature of 800 °C compromised the integrity of the steel fibers, leading to a further reduction in the flexural strength of UHPdC.

Fig. 12 shows change in color of steel fibres inside sand, barite and magnetite UHPdC. Steel fibres appear black due to severe

oxidation which is also observed in study of steel fibre's morphologies at high temperature [73]. The study also reports that steel fibre losses its structural integrity at this temperature due to cracking and peeling from the oxidation process. This resulted in lower reinforcing effect from steel fibre hence lower flexural strength of UHPdC. Furthermore, it is revealed that incorporating steel fibers into concrete is regarded as a highly effective strategy for mitigating spalling risks and bolstering mechanical properties [69].

Steel fibers are essential in preventing spalling; however, their effect on the residual compressive strength after heat exposure is limited [74]. Incorporating steel fibers increases the ultimate strain, thereby enhancing the compressive strength and ductility of the concrete [75]. Moreover, steel fibers contribute to higher compressive strength, improved flexural strength, and an increased elastic modulus. These enhancements collectively improve the ductility of the concrete and help limit crack propagation [76]. The residual compressive strength in high-strength concrete, with steel fiber content ranging from 1 % to 3 %, rises when heated at temperatures between 200 and 300°C. However, this strength diminishes considerably at temperatures above 300°C [77]. Concrete specimens embedded with short steel fibers demonstrate enhanced tensile strength, while those with longer fibers exhibit greater ultimate strain compared to their shorter-fiber counterparts [78].

### 3.1.3. Residual splitting tensile strength

Overall, the elevated temperature resulted in a significant reduction in both the flexural and splitting tensile strength of all ultra-high-performance concrete (UHPdC) samples. This decline in mechanical properties can be attributed to the degradation of cement hydration products within the concrete matrix. The high temperatures caused a breakdown of these hydration products, leading to a compromised microstructure. Consequently, the integrity of the concrete was adversely affected, resulting in poorly structured material. Moreover, the weakened microstructure diminished the interlocking capability of the steel fibers embedded within the concrete, further contributing to the reduction in overall strength and durability [79,80]. In terms of residual splitting tensile strength, sand UHPdC recorded the highest value at 14.2 MPa, followed by magnetite UHPdC at 13.5 MPa after exposure to 400°C (Fig. 13).

The lowest splitting tensile strength at the same temperature was recorded by barite UHPdC at 11.9 MPa. Regarding the percentage reduction in strength due to heating at 400°C, sand, magnetite, and barite UHPdC showed decreases of 19.2 %, 10.9 %, and 17.5 % respectively. At 800°C, these materials exhibited even larger reductions in splitting tensile strength, with percentages of 80.2 %, 74.9 %, and 81.9 % respectively. After exposure to 800°C, the residual splitting tensile strengths recorded were 3.5 MPa for sand, 3.8 MPa for magnetite, and 2.6 MPa for barite UHPdC. This trend mirrors the results for flexural strength, where the reduction in strength for sand UHPdC was greater after exposure to 800°C compared to 400°C.

The reduction in structural integrity is primarily due to the phase transition of quartz in the sand, which occurs beyond 570°C. At this temperature, quartz undergoes a transformation from alpha-quartz to beta-quartz, resulting in a significant volume change and the development of internal stresses that contribute to microcracking within the concrete matrix [60]. Furthermore, barite UHPdC exhibited a substantial reduction in splitting tensile strength with increased heat exposure. This reduction is linked to the high thermal expansion coefficient of barite aggregate, which exacerbates the deterioration of the microstructural integrity. Magnetite UHPdC, on the other hand, demonstrated the highest thermal stability, as indicated by its residual strength values, which are consistent with the results observed in flexural strength tests.

It has been observed that the splitting tensile strength of concrete specimens significantly declines after initial heating, highlighting the impact of thermal exposure on the mechanical properties of UHPdC [81]. This reduction is due to multiple factors including steam pressure generated by water within the concrete, thermal stress caused by temperature variations, and the degradation of concrete from the decomposition of specific hydrates [82]. Further reports indicate that if thermal stress exceeds the concrete's tensile strength, fractures occur [63].

Moreover, the steam pressure hypothesis suggests that high internal steam pressure can cause concrete to crack [83]. It is revealed that both theories highlight that concrete damage is influenced by internal thermal stress and vapor pressure, alongside the material's

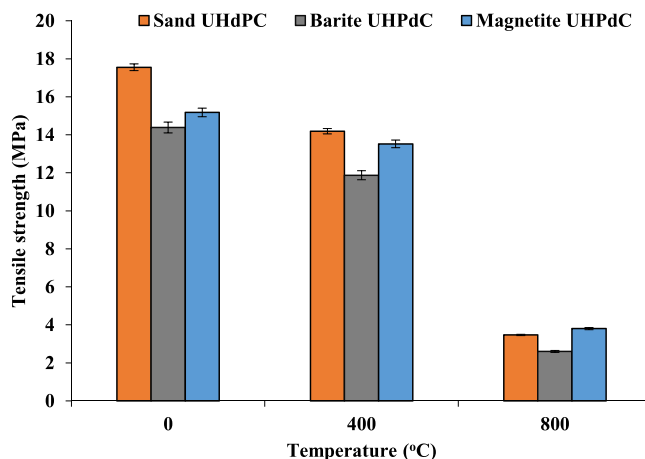


Fig. 13. Effect of temperature on splitting tensile strength of optimised sand, barite and magnetite UHPdC.

capacity to resist these forces [63]. In conclusion, the tensile properties of concrete are vital in assessing the potential for brittle damage, which greatly affects the formation of cracks and the overall durability of concrete structures [84]. These factors collectively lead to a significant decrease in the splitting tensile strength of the concrete.

### 3.2. Radiation shielding properties of UHPdC

#### 3.2.1. Residual linear attenuation coefficient

In terms of the linear attenuation coefficient, magnetite UHPdC recorded the highest residual shielding value following exposure to Cs-137 after heating at 400°C, at 0.1889 cm<sup>-1</sup> (Fig. 14). This represents a 4.2 % reduction compared to the unheated sample, the lowest reduction recorded among all UHPdC types. Barite and sand UHPdC each recorded a 7.5 % reduction, indicating their poorer thermal durability compared to magnetite UHPdC. An increase in temperature to 800°C led to a further decrease in the linear attenuation coefficient for sand UHPdC, which recorded 0.15 cm<sup>-1</sup>, 2.4 % lower than the value after exposure to 400°C. In contrast, barite and magnetite UHPdC exhibited only minimal reductions of 0.06 % and 0.11 %, respectively. This suggests that temperatures exceeding 400°C significantly degrade the shielding effectiveness of sand UHPdC [85]. The deterioration is likely due to severe cracking and phase transitions in the quartz within the sand aggregate, resulting in reduced density and overall shielding properties. When using a Co-60 radiation source, which has a higher energy level than Caesium-137, a more substantial reduction in the linear attenuation coefficient was observed in samples heated to 400°C (Fig. 15).

Magnetite, barite, and sand UHPdC recorded reductions of 6.4 %, 6.1 %, and 6.7 %, respectively. Further reductions in shielding value due to heat at 800°C were only observed in sand UHPdC, at 2.8 %, a figure similar to that shown in tests with Cs-137. It is well-known that the difference in energy levels between Co-60 and Cs-137 affected the LAC values of the concrete types. The higher energy level of Co-60 resulted in a lower shielding effectiveness. This phenomenon may be attributed to the intensive cracking observed in the sand, as well as the phase transition of quartzite within the sand aggregate. At a temperature of approximately 570°C, quartz undergoes a phase transition from alpha-quartz ( $\alpha$ -quartz) to beta-quartz ( $\beta$ -quartz) [60]. This transition is accompanied by a volume expansion and a change in the crystal structure, which can induce further cracking and reduce the material's density. These factors collectively contribute to a reduction in the material's density and a consequent decrease in its overall shielding properties.

Based on this study, magnetite UHPdC shows superior performance of gamma ray shielding compared to other UHPdC. This is due to denser composition with presence of iron, Fe which resulted in higher shielding. Based on past research of magnetite-based RSC [45], the maximum  $\mu$  value of 0.295 cm<sup>-1</sup> was recorded for a concrete mix composed solely of coarse and fine magnetite, with a density of 3320 kg/m<sup>3</sup> [70]. However, another sample with a slightly higher density of 3378.3 kg/m<sup>3</sup> exhibited a lower  $\mu$  value of 0.228 cm<sup>-1</sup> [19]. This reduction may stem from the use of less pure magnetite, which showed iron oxide (Fe<sub>3</sub>O<sub>4</sub>) content between 72.1 % and 78.2 %, compared to the 90 % content typically used in studies. Further investigations revealed that an increased water-to-cement ratio in magnetite concrete reduces its  $\mu$  value, highlighting the impact of mixture ratios on the shielding effectiveness [19,70].

#### 3.2.2. Residual macroscopic removal cross section

In the context of neutron shielding, the residual macroscopic removal cross section is a critical parameter that quantifies the effectiveness of a material in attenuating neutron radiation. However, this study does not calculate the macroscopic removal cross section based on atomic mass because the calculated values from standard databases, such as the National Institute of Standards and Technology (NIST) database. This is because the macroscopic removal cross section value based on the atomic number of elements are

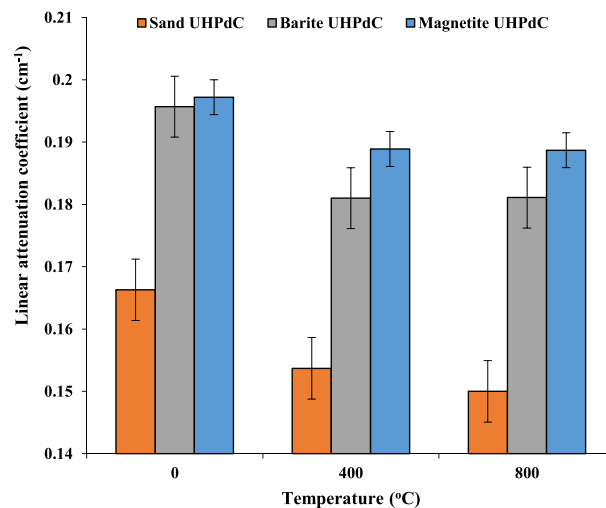


Fig. 14. Linear attenuation coefficient values recorded based on increasing temperature and Cs-137 exposure.

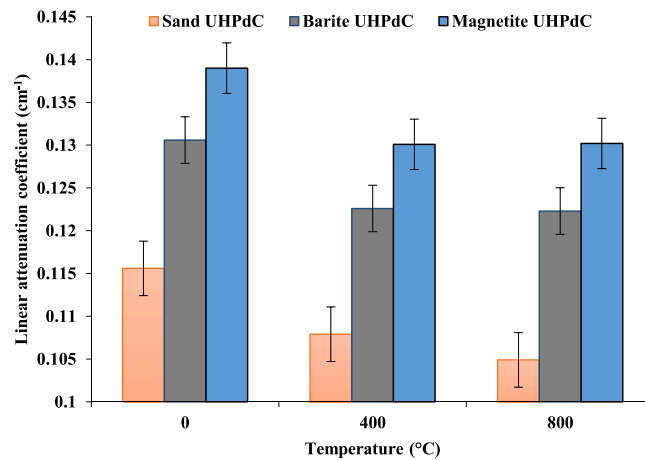


Fig. 15. Linear attenuation coefficient values recorded based on increasing temperature and Co-60 exposure.

derived from fast neutrons in the range of 2–12 MeV, while this study uses an AmBe source with a different energy level. Another method of calculating macroscopic removal cross section value based on NIST database is also not employed in this study. The calculated values from the database show a large deviation from the experimental work. This discrepancy is largely due to the difference in neutron behavior, as the NIST database is based on thermal neutrons with a velocity of 2200 m/s at 293.6 K, corresponding to an energy of 0.0253 eV, whereas this study uses AmBe neutrons with an energy of 4.5 MeV. Consequently, the neutron shielding values derived from the NIST database are not applicable to the conditions and neutron energy levels used in this study.

In terms of neutron shielding, magnetite UHPdC consistently recorded the highest values throughout the temperature exposures. Heating at 400°C resulted in an 8.1 % reduction in neutron shielding for magnetite UHPdC, corresponding to a  $0.0282 \text{ cm}^{-1}$  decrease in the macroscopic removal cross-section,  $\sum_R(E_n)$  (Fig. 16). Sand and barite UHPdC exhibited reductions of 9.5 % and 15.9 % in  $\sum_R(E_n)$  respectively, indicative of their lower thermal stability compared to magnetite UHPdC. The expansion of sand and barite within the UHPdC induces cracking and allows greater evaporation of bonded water, as well as deterioration of colemanite, resulting in diminished neutron shielding [86].

At the elevated temperature of 800°C, all samples exhibited smaller reductions in neutron shielding effectiveness, indicating that most neutron moderators and absorbers had already been removed at 400°C. Specifically, magnetite UHPdC showed only a 1.8 % decrease in the removal cross-section value compared to the sample exposed to 400°C. Similarly, barite UHPdC exhibited a 2.2 % reduction, while sand UHPdC recorded the largest reduction of 4.2 %. This behavior can also be attributed to the evaporation of chemically bound water within the concrete matrix at high temperatures. The loss of this water leads to a decrease in hydrogen content, which is a key component in neutron moderation. Consequently, the reduction in hydrogen content diminishes the neutron shielding capability of the UHPdC, particularly at temperatures beyond 400°C. Overall, magnetite UHPdC demonstrates the greatest durability against temperatures up to 800°C in terms of neutron shielding value, followed by sand UHPdC, and lastly barite UHPdC.

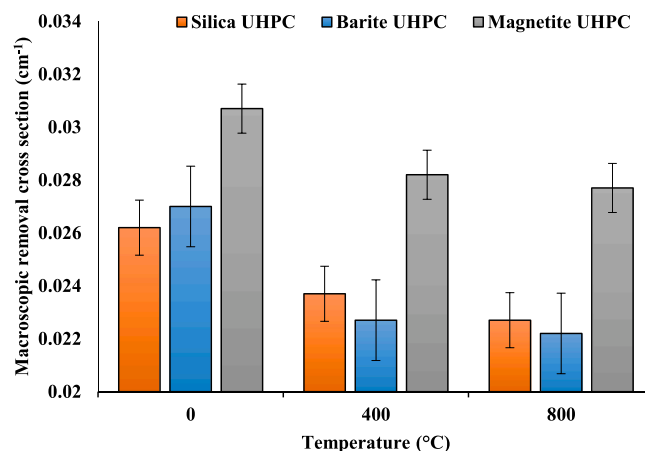


Fig. 16. Effect of temperature exposure on macroscopic removal cross section of UHPdC.

### 3.3. An X-ray $\mu$ -CT scan

Despite advancements in modern X-ray micro-computed tomography (X-ray  $\mu$ -CT) technology, powerful computing capabilities, and sophisticated image processing methods, analyzing  $\mu$ -CT images of UHPdC presents several challenges. The dense arrangement of short fibers within UHPC complicates image analysis due to the fibers being tightly packed together in a confined space, often resulting in fibers touching each other. Moreover, the bleeding effect in the tomograms of UHPdC makes the fibers appear thicker, which further complicates the distinction between them in the images.  $\mu$ -CT imaging typically requires smaller samples, necessitating multiple samples from various parts of a structure to adequately assess fiber dispersion throughout. This underscores the necessity for more streamlined and automated approaches in the  $\mu$ -CT image analysis of UHPdC structures.

Sample of optimised UHPdCs are analyzed using x-ray  $\mu$ -CT scan for non-intrusive analysis. Based on the x-ray scan of the sample, internal structure and reconstruction of three-dimensional models were produced for analysis. However, only magnetite and sand UHPdC produced viable results while barite UHPdC shows indistinguishable internal structure from the x-ray  $\mu$ -CT (Fig. 17). This is due to absorption edge of barite in the lower energy region that may absorb large amount of x-ray which prevent any detection [87]. The  $\mu$ -CT scanned images of barite UHPdC samples appear indistinguishable due to the absorption edge of barite. The absorption edge, specifically the K-absorption edge, refers to the abrupt increase in the photoelectric absorption of X-ray photons at an energy level just beyond the binding energy of the K-shell electrons of the absorbing atom. K-shell electrons are the innermost electrons in an atom, and their binding energy is unique to each element. In the case of barite, this high absorption at the K-edge results in a significant attenuation of X-rays, making it challenging to differentiate internal structures in the scanned images. It is important to note that this indistinguishability is not due to poor sampling or imaging techniques but is an inherent property of barite's interaction with X-rays at specific energy levels. Furthermore, fine size of barite in comparison to magnetite reduce the gap between high density aggregate which prevent x-rays penetration that produce images [88].

X-ray  $\mu$ -CT scans were utilized in this study to reveal the internal structure of UHPdC samples. The scanned images facilitated a detailed analysis of fibre orientation in both unheated and heated samples. Results indicated that heating did not significantly affect the fibre orientation within the UHPdC. Moreover, the non-destructive nature of  $\mu$ -CT scanning allowed for the precise analysis of pores induced by heating, providing valuable insights into the material's microstructural changes without compromising the integrity of the samples. Fig. 18 shows the reconstructed 3D model of unheated and heated sand UHPdC. Based on the model, steel fibres are well oriented as indicated by red and green line. Heated sand UHPdC indicates a large amount of steel fibres oriented perpendicular to direction of casting which is beneficial in resisting flexural deformation. This is also shown in magnetite UHPdC which most of steel fibres in unheated and heated samples are positioned in perpendicular to direction of casting (Fig. 19). This resulted in higher strength of flexural member such as beam and slab. The 3D model of magnetite UHPdC also showed a slightly lighter grey of concrete in heated sample compared to unheated sample. This indicated a reduction in density of magnetite UHPdC due to heating at 800 °C which congruent with lower shielding properties of heated sample compared to unheated sample.

It is well-known that fiber orientation impacts the mechanical performance characteristics of UHPC, with research indicating that while the fiber's volume fraction does not markedly influence UHPC's elastic properties, their orientation does [89,90]. Researchers have calculated the orientation angle of fibers in relation to a central global axis, using these angles to determine a comprehensive orientation factor [91]. Furthermore, previous studies have observed crack healing in UHPC at 1000°C, attributed to the C-S-H gel's transformation into calcium silicate ( $\text{CaSiO}_3$ ), a process termed decalcification. At this extreme temperature, crack healing process involves the depletion of calcium ions, forming a dense, impermeable  $\text{CaSiO}_3$  layer that effectively seals cracks [92–94]. In particular, at 1000°C, hybrid steel-basalt fiber reinforced UHPC exhibited significant crack healing, in contrast to standard UHPC where healing was absent due to extensive crack propagation. This phenomenon, known as autogenous self-healing, is generally limited to smaller cracks under 100 microns [95].

Analysis on constructed cross section of unheated sand UHPdC shows pores formation adjacent to steel fibres (Fig. 20a). This indicated that a fibre in UHPdC contributes to formation of pores which lead to lower strength. Furthermore, pores are also formed along the orientation of steel fibres that would affect adhesion between cement paste and steel fibre (Fig. 20a). For heated sand UHPdC sample, slice image from side of the sample shows intensive cracking formed around sand which is due to expansion of sand at 800 °C (Fig. 21a). Furthermore, these cracks are also found to be connected between pores which help diffuse internal pressure due to heat, hence preventing spalling. Formations of cracks are also found in along steel fibre orientation which may be due to the expansion of the fibre and deterioration of cement paste (Fig. 21b). This resulted in less adhesion between fibres and hardened cement paste hence congruent with lower flexural strength observed in heated sample compared to unheated sample.

From Fig. 21a, also, it is exhibited that the side cross-section is annotated with measurements of various regions, presumably to indicate the scale of microcracks or voids that have emerged post-heating. The multiplicity of scales, from 0.05 mm to 0.22 mm, suggests a non-uniform response to thermal stress, likely caused by differential thermal expansion or contraction of the material components. This non-uniformity may increase the material's vulnerability to mechanical failure when subjected to load, as microcracks can propagate under stress. In Fig. 21b, it is showed that the green overlays could be indicative of specific analyses performed, such as highlighting areas of maximum damage or mapping crack propagation pathways. These features are critical as they provide insights into the directional tendencies of crack formation and growth, which are essential for predicting the material's behavior under continued thermal stress or mechanical loading.

Reportedly, it is revealed that increased yield stress enhances the resistance to segregation of steel fibers throughout the compaction process [96]. Furthermore, increasing the quantity of steel fibers results in a more uniform fiber distribution. This enhancement is likely due to improved interaction and mechanical interlocking among the fibers [96], which helps stabilize the fresh concrete mixture. A similar pattern has been observed in normal strength concrete [97]. The reduction in pore volume during mixture

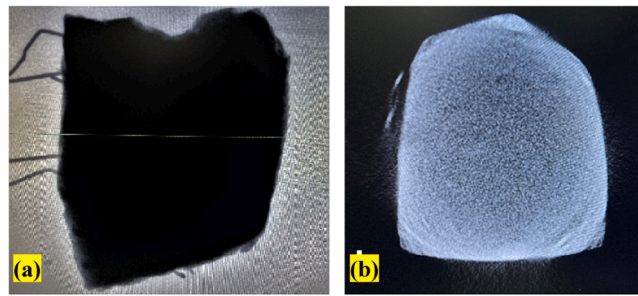


Fig. 17. Photos of (a) an X-ray  $\mu$ -CT scanned and (b) constructed slice of barite UHPdC.

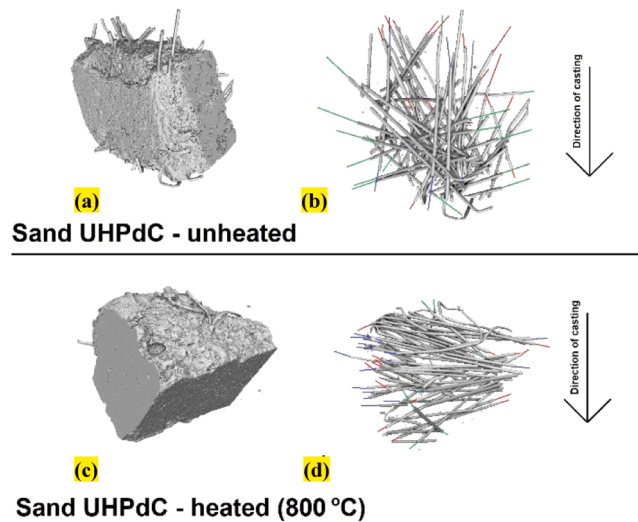


Fig. 18. An X-ray  $\mu$ -CT 3D-reconstructed image of [unheated (a) 3D model and (b) steel fibers] and [heated (c) 3D model and (d) steel fibers] sample of sand UHPdC.

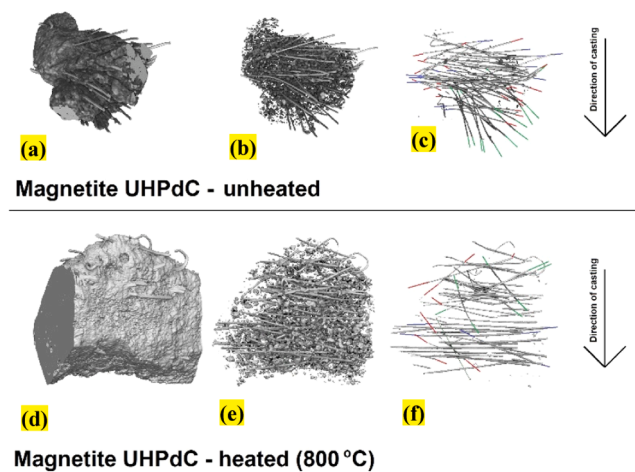


Fig. 19. An X-ray  $\mu$ -CT 3D-reconstructed image of [unheated (a) 3D model, (b) matrix-steel fibers and (c) steel fibers] and [heated (a) 3D model, (b) matrix-steel fibers and (c) steel fibers] sample of magnetite UHPdC.

preparation is attributed to the fibers breaking down larger air bubbles [98].

For the UHPdC containing magnetite, crack formation is less prevalent; however, similar to sand UHPdC, cracks connecting the pores are also observed (Fig. 22c). Nonetheless, these cracks are less conspicuous compared to those in sand UHPdC, which suggests a

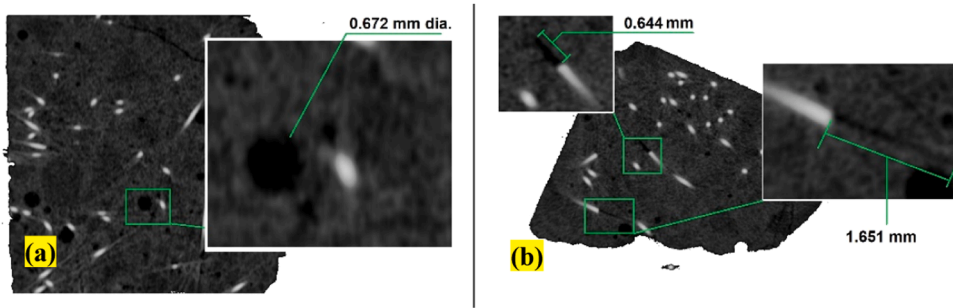


Fig. 20. An X-ray  $\mu$ -CT image of (a) side and (b) top cross-section of unheated sand UHPdC.

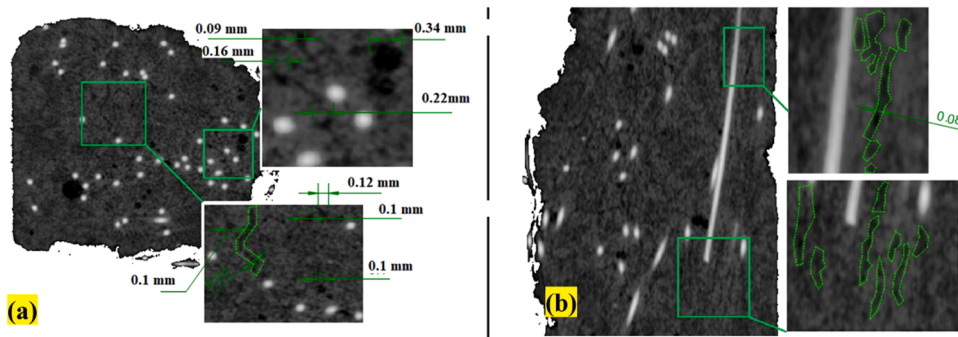


Fig. 21. An X-ray  $\mu$ -CT image of (a) side and (b) top cross-section of 800 °C heated sand UHPdC.

lesser severity. This reduced visibility of cracks in magnetite UHPdC may be attributed to the greater thermal stability of magnetite compared to sand. Moreover, slice imaging revealed that cracks originate from pores, suggesting pore expansion due to pressure build-up caused by increasing heat, which subsequently leads to cracking. Such cracking adjacent to pores is absent in the unheated samples of magnetite UHPdC, as depicted in Fig. 22a.

Analysis of the unheated magnetite samples also reveals pore formation adjacent to steel fibers, a phenomenon also observed in sand UHPdC (Fig. 22b). This suggests that the incorporation of fibers contributes to an increased pore volume. Moreover, magnetite aggregate is more conspicuous than sand aggregate in the images, owing to the higher density of magnetite relative to other constituents in UHPdC. Observations from heated samples indicate that cracks form around the magnetite aggregates, thereby demonstrating that no discernible cracking occurs within the magnetite itself upon heating to 800°C. The heating of UHPdC leads to crack formation due to aggregate expansion, deterioration of the cement paste, and evaporation of fibers. CT-scan results further substantiate that magnetite UHPdC exhibits superior thermal durability compared to sand UHPdC, evidenced by less apparent cracking in the images.

Minimizing temperature gradients is essential for reducing thermal stress-induced cracks in the UHPC matrix, thereby improving its mechanical properties [99]. Variations in micromechanical properties within the same phase can occur due to the heterogeneous nature of cement hydration [100]. It is important to note that the average mechanical properties obtained from nanoindentation tests may not accurately reflect the effective properties of UHPC due to the limited number of samples [101]. Moreover, the dense microstructure of the UHPC matrix helps retain moisture, resulting in significantly lower mass loss, less than 25 %, compared to the typical 70 % seen in standard concrete under similar conditions [102]. At approximately 200°C, the removal of water, the increase in surface forces, and the buildup of pore pressure collectively contribute to an approximate 5 % increase in the compressive strength of UHPC [103]. However, this dense microstructure can also hinder moisture migration, making plain UHPC vulnerable to stress from pore pressure [104]. Moreover, a high heating rate can induce excessive thermal stress within the UHPC matrix [105]. The combined effects of pore pressure and thermal stress can lead to explosive spalling, which compromises structural integrity and increases thermal damage, thus accelerating heat transfer within the matrix [99]. Further research is needed to explore the effects of hybrid fibers in UHPC on both static and dynamic mechanical properties at high temperatures. Observations of failure modes under compression suggest that the softening of the UHPC matrix is mitigated by the inclusion of steel or hybrid fibers.

#### 4. Conclusions

This research project emphasized the superior performance of magnetite UHPdC in radiation shielding and mechanical resilience. Magnetite UHPdC exhibits outstanding neutron shielding, surpassing barite UHPdC by 17.6 % and sand UHPdC by 17.2 %, and provides the most effective gamma ray shielding against Co-60, outperforming barite by 22.5 % and sand by 12.1 %. The high density

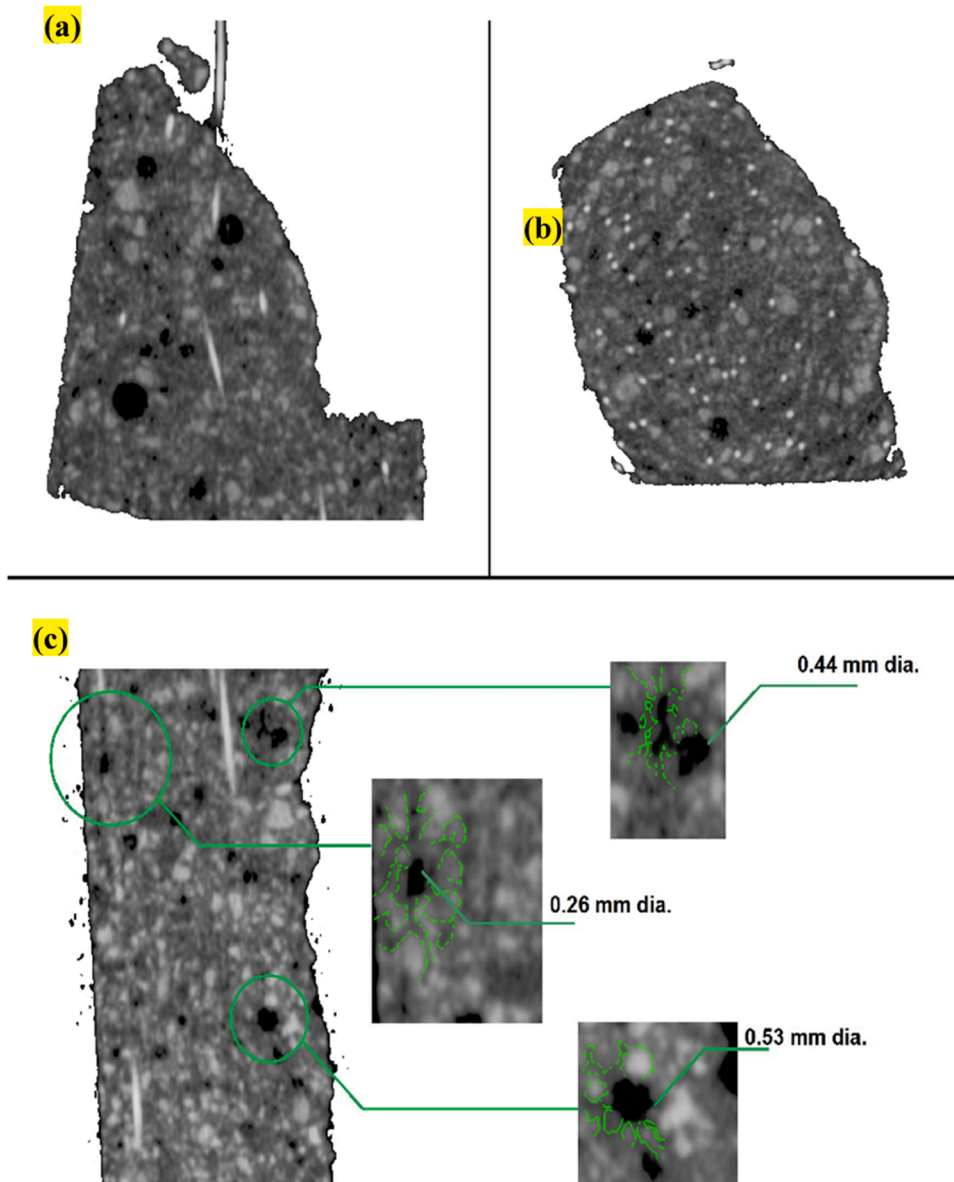


**Fig. 22.** An X-ray  $\mu$ -CT image of (a) top and (b) side cross-section of unheated magnetite UHPdC along with (c) image of front cross-section of 800 °C heated magnetite UHPdC.

of magnetite significantly enhances its shielding capabilities, making it a prime candidate for nuclear safety applications. The mechanical properties of UHPdC are influenced by several factors, including aggregate type, thermal exposure, and the presence of fibers. Sand UHPdC achieves the highest compressive strength at 131.0 MPa, but its performance deteriorates at high temperatures due to aggregate expansion and cracking. In contrast, magnetite UHPdC maintains better mechanical integrity under thermal stress, showing the least reduction in flexural strength up to 800°C. The expansion of aggregates like sand and barite at high temperatures leads to cracking and a significant reduction in compressive and tensile strengths. Moreover, the high thermal expansion coefficient of barite compromises its microstructural integrity, resulting in lower splitting tensile strength. The study also highlights the role of oriented steel fibers in enhancing flexural deformation resistance, although pore formation along these fibers can impact adhesion with the cement paste. Overall, the findings emphasize the need for continued research to optimize UHPdC's performance, particularly in enhancing its gamma-neutron shielding effectiveness and mechanical properties under various operational conditions.

#### CRediT authorship contribution statement

**Raizal S.M. Rashid:** Writing – review & editing, Visualization, Validation, Supervision, Resources, Methodology, Formal analysis,

Data curation. **Muhd Afiq Hizami Abdullah**: Writing – review & editing, Writing – original draft, Methodology, Investigation, Formal analysis, Data curation, Conceptualization. **Abdullah Alnutayfat**: Writing – review & editing, Writing – original draft, Visualization, Software, Funding acquisition, Formal analysis, Data curation, Conceptualization.

## Declaration of Competing Interest

The authors declare that they have no known competing financial interests or personal relationships that could have appeared to influence the work reported in this paper.

## Acknowledgment

The authors extend their appreciation to Prince Sattam bin Abdulaziz University for funding this research work through the project number (PSAU/2024/01/29630).

## Data availability

The authors do not have permission to share data.

## References

- [1] M.D. Mathew, Nuclear energy: a pathway towards mitigation of global warming, *Prog. Nucl. Energy* 143 (2022), <https://doi.org/10.1016/j.pnucene.2021.104080>.
- [2] K. Park, H.T. Kim, T.H. Kwon, E. Choi, Effect of neutron irradiation on response of reinforced concrete members for nuclear power plants, *Nucl. Eng. Des.* 310 (2016) 15–26, <https://doi.org/10.1016/j.nucengdes.2016.09.034>.
- [3] K. Sadamori, Nuclear power in a clean energy system, *Ann. Des. Mines - Responsab. Environ.* (2019) 122–126, <https://doi.org/10.3917/re1.097.0122>.
- [4] IEA-agency, Cumulative CO2 emissions avoided by nuclear power by country, 1990-2020, Int. Energy Agency Website (2019) 1. (<https://www.iea.org/data-and-statistics/charts/cumulative-co2-emissions-avoided-by-global-nuclear-power-in-selected-countries-1971-2018>).
- [5] B. Pomaro, A review on radiation damage in concrete for nuclear facilities: from experiments to modeling, *Model. Simul. Eng.* 2016 (2016), <https://doi.org/10.1155/2016/4165746>.
- [6] L.H. Roddis, Nuclear power in the world today, *IEEE Spectr.* 2 (1965) 90–97, <https://doi.org/10.1109/MSPEC.1965.5531714>.
- [7] L.H. Roddis, Nuclear power in the world today, *World Nucl. Assoc. Website* 2 (2023), <https://doi.org/10.1109/MSPEC.1965.5531714>.
- [8] A. McDonald, Nuclear power: global status, *IAEA Bull.* 49 (2008) 45–48.
- [9] World-Nuclear-Power-Reactors, World Nuclear Power Reactors and Uranium Requirements, World Nucl. Assoc. London. (2014).
- [10] L. Rečka, M. Ščasný, Brown coal and nuclear energy deployment: effects on fuel-mix, carbon targets, and external costs in the Czech Republic up to 2050, *Fuel* 216 (2018) 494–502, <https://doi.org/10.1016/j.fuel.2017.12.034>.
- [11] F. Sanchez, Development of nano-modified concrete for next generation of storage systems, *Sci. / Tech. Rep. Intellect. Prop.* (2018), <https://doi.org/10.2172/1469196>.
- [12] Y. Reches, A multi-scale review of the effects of gamma radiation on concrete, *Results Mater.* 2 (2019) 100039, <https://doi.org/10.1016/j.rinma.2019.100039>.
- [13] A.S. Ouda, Development of high-performance heavy density concrete using different aggregates for gamma-ray shielding, *Prog. Nucl. Energy* 79 (2015) 48–55, <https://doi.org/10.1016/j.pnucene.2014.11.009>.
- [14] M. Demir, H.S. Gümüř, Gökçe, Gamma ray and neutron shielding characteristics of polypropylene fiber-reinforced heavyweight concrete exposed to high temperatures, *Constr. Build. Mater.* 257 (2020), <https://doi.org/10.1016/j.conbuildmat.2020.119596>.
- [15] A. Mesbahi, G. Alizadeh, G. Seyed-Oskoe, A.A. Azarpeyvand, A new barite-colemanite concrete with lower neutron production in radiation therapy bunkers, *Ann. Nucl. Energy* 51 (2013) 107–111, <https://doi.org/10.1016/j.anucene.2012.07.039>.
- [16] O. Aksohan, H. Binici, E. Ortlek, Durability of concrete made by partial replacement of fine aggregate by colemanite and barite and cement by ashes of corn stalk, wheat straw and sunflower stalk ashes, *Constr. Build. Mater.* 106 (2016) 253–263, <https://doi.org/10.1016/j.conbuildmat.2015.12.102>.
- [17] M.K.A. Roslan, M. Ismail, A.B.H. Kueh, M.R.M. Zin, High-density concrete: Exploring Ferro boron effects in neutron and gamma radiation shielding, *Constr. Build. Mater.* 215 (2019) 718–725, <https://doi.org/10.1016/j.conbuildmat.2019.04.105>.
- [18] N.M. Azreen, R.S.M. Rashid, Y.H. Mugahed Amran, Y.L. Voo, M. Haniza, M. Hairie, R. Alyousef, H. Alabduljabbar, Simulation of ultra-high-performance concrete mixed with hematite and barite aggregates using Monte Carlo for dry cask storage, *Constr. Build. Mater.* 263 (2020), <https://doi.org/10.1016/j.conbuildmat.2020.120161>.
- [19] O. Lotfi-Omran, A. Sadrmomtazi, I.M. Nikbin, A comprehensive study on the effect of water to cement ratio on the mechanical and radiation shielding properties of heavyweight concrete, *Constr. Build. Mater.* 229 (2019), <https://doi.org/10.1016/j.conbuildmat.2019.116905>.
- [20] A.M. Zayed, M.A. Masoud, A.M. Rashad, A.M. El-Khayatt, K. Sakr, W.A. Kansouh, M.G. Shahien, Influence of heavyweight aggregates on the physico-mechanical and radiation attenuation properties of serpentine-based concrete, *Constr. Build. Mater.* 260 (2020) 120473, <https://doi.org/10.1016/j.conbuildmat.2020.120473>.
- [21] M.U. Khan, S. Ahmad, A.A. Naqvi, H.J. Al-Gahtani, Shielding performance of heavy-weight ultra-high-performance concrete against nuclear radiation, *Prog. Nucl. Energy* 130 (2020), <https://doi.org/10.1016/j.pnucene.2020.103550>.
- [22] A.M. Zayed, A.M. El-Khayatt, P. Petrounias, M.G. Shahien, K.A. Mahmoud, A.M. Rashad, A.H. Ragab, A.A. Hassan, B.R. Bakhit, M.A. Masoud, From discarded waste to valuable products: barite combination with chrysotile mine waste to produce radiation-shielding concrete, *Constr. Build. Mater.* 417 (2024) 135334.
- [23] I. Maruyama, O. Kontani, S. Sawada, O. Sato, G. Igarashi, M. Takizawa, Evaluation of irradiation effects on concrete structure-background and preparation of neutron irradiation test, *Am. Soc. Mech. Eng. Power Div. Power* 2 (2013), <https://doi.org/10.1115/POWER2013-98114>.
- [24] I. Maruyama, O. Kontani, M. Takizawa, S. Sawada, S. Ishikawa, J. Yasukouchi, O. Sato, J. Etoh, T. Igari, Development of soundness assessment procedure for concrete members affected by neutron and gamma-ray irradiation, *J. Adv. Concr. Technol.* 15 (2017) 440–523, <https://doi.org/10.3151/jact.15.440>.
- [25] F. Vodák, K. Trtík, V. Sopko, O. Kapicková, P. Demo, Effect of  $\gamma$ -irradiation on strength of concrete for nuclear-safety structures, *Cem. Concr. Res.* 35 (2005) 1447–1451, <https://doi.org/10.1016/j.cemconres.2004.10.016>.
- [26] P. Sikora, M. Chougan, K. Cuevas, M. Liebscher, V. Mechtcherine, S.H. Ghaffar, M. Liard, D. Lootens, P. Krivenko, M. Sanysky, D. Stephan, The effects of nano- and micro-sized additives on 3D printable cementitious and alkali-activated composites: a review, *Appl. Nanosci.* (2021), <https://doi.org/10.1007/s13204-021-01738-2>.
- [27] I. Maruyama, S. Ishikawa, J. Yasukouchi, S. Sawada, R. Kurihara, M. Takizawa, O. Kontani, Impact of gamma-ray irradiation on hardened white Portland cement pastes exposed to atmosphere, *Cem. Concr. Res.* 108 (2018) 59–71, <https://doi.org/10.1016/j.cemconres.2018.03.005>.

- [28] M.A. Masoud, A.M. El-Khayatt, K.A. Mahmoud, A.M. Rashad, M.G. Shahien, B.R. Bakhit, A.M. Zayed, Valorization of hazardous chrysotile by H<sub>3</sub>BO<sub>3</sub> incorporation to produce an innovative eco-friendly radiation shielding concrete: Implications on physico-mechanical, hydration, microstructural, and shielding properties, *Cem. Concr. Compos.* 141 (2023), <https://doi.org/10.1016/j.cemconcomp.2023.105120>.
- [29] L. Chang, Y. Zhang, Y. Liu, J. Fang, W. Luan, X. Yang, W. Zhang, Preparation and characterization of tungsten/epoxy composites for  $\gamma$ -rays radiation shielding, *Nucl. Instrum. Methods Phys. Res. Sect. B Beam Interact. Mater. At.* 356–357 (2015) 88–93, <https://doi.org/10.1016/j.nimb.2015.04.062>.
- [30] Y. Reches, Nanoparticles as concrete additives: Review and perspectives, *Constr. Build. Mater.* 175 (2018) 483–495, <https://doi.org/10.1016/j.conbuildmat.2018.04.214>.
- [31] A.G. Pérez-Luna, A.L. Martínez-Hernández, G. Martínez-Barrera, C. Velasco-Santos, Nanoreinforced concrete: Effect Of gamma-irradiated SiO<sub>2</sub> nanoparticles, *Adv. Mater. Lett.* 7 (2016) 156–162, <https://doi.org/10.5185/amlett.2016.6145>.
- [32] D.L. Fillmore, Literature Review of the Effects of Radiation and Temperature on the Aging of Concrete - Prepared for the Central Research Institute of Electric Power Institute - INEEL/EXT-04-02319, (2004) 1–16.
- [33] M.F. Kaplan, *Concrete radiation shielding: nuclear physics, concrete properties, design and construction*, Longman Sci. Tech. (1989).
- [34] Y. Reches, K. Thomson, M. Helbing, D.S. Kosson, F. Sanchez, Agglomeration and reactivity of nanoparticles of SiO<sub>2</sub>, TiO<sub>2</sub>, Al<sub>2</sub>O<sub>3</sub>, Fe<sub>2</sub>O<sub>3</sub>, and clays in cement pastes and effects on compressive strength at ambient and elevated temperatures, *Constr. Build. Mater.* 167 (2018) 860–873, <https://doi.org/10.1016/j.conbuildmat.2018.02.032>.
- [35] M. Hassanzadeh, S.M. Sadat Kiai, Calculation of photon attenuation coefficient and dose rate in concrete with the addition of SiO<sub>2</sub> and MnFe<sub>2</sub>O<sub>4</sub> nanoparticles using MCNPX code and comparison with experimental results, *Nucl. Sci. Tech.* 29 (2018), <https://doi.org/10.1007/s41365-018-0493-y>.
- [36] B. Pomaro, V.A. Salomoni, F. Gramegna, G. Prete, C.E. Majorana, Radiation damage evaluation on concrete within a facility for Selective Production of Exotic Species (SPES Project), Italy, *J. Hazard. Mater.* 194 (2011) 169–177, <https://doi.org/10.1016/j.jhazmat.2011.07.079>.
- [37] Y. Jing, Y. Xi, Long-term neutron radiation levels in distressed concrete biological shielding walls, *J. Hazard. Mater.* 363 (2019) 376–384, <https://doi.org/10.1016/j.jhazmat.2018.09.080>.
- [38] Y. Le Pape, A. Giorla, J. Sanahuja, Combined Effects Of Temperature And Irradiation On Concrete Damage, *J. Adv. Concr. Technol.* 14 (2016) 70–86, <https://doi.org/10.3151/jact.14.70>.
- [39] K. Zalewski, T. Piotrowski, A. Garbac, G. Adamczewski, Relation between microstructure, technical properties and neutron radiation shielding efficiency of concrete, *Constr. Build. Mater.* 235 (2020), <https://doi.org/10.1016/j.conbuildmat.2019.117389>.
- [40] B. Kanagaraj, N. Anand, A. Diana Andrushia, M.Z. Naser, Recent developments of radiation shielding concrete in nuclear and radioactive waste storage facilities – A state of the art review, *Constr. Build. Mater.* 404 (2023), <https://doi.org/10.1016/j.conbuildmat.2023.133260>.
- [41] A. Arora, Y. Yao, B. Mobasher, N. Neithalath, Fundamental insights into the compressive and flexural response of binder- and aggregate-optimized ultra-high performance concrete (UHPC), *Cem. Concr. Compos.* 98 (2019) 1–13, <https://doi.org/10.1016/j.cemconcomp.2019.01.015>.
- [42] T.E. Allard, M.W. Priddy, I.L. Howard, J. Shannon, Isothermal strength development models of ultra-high-performance concrete, *Acids Mater. J.* 117 (2020) 175–185, <https://doi.org/10.14359/51719075>.
- [43] M. Shafieifar, M. Farzad, A. Azizinamini, Experimental and numerical study on mechanical properties of Ultra High Performance Concrete (UHPC), *Constr. Build. Mater.* 156 (2017) 402–411, <https://doi.org/10.1016/j.conbuildmat.2017.08.170>.
- [44] M.A. Masoud, W.A. Kansouh, M.G. Shahien, K. Sakr, A.M. Rashad, A.M. Zayed, An experimental investigation on the effects of barite/hematite on the radiation shielding properties of serpentine concretes, *Prog. Nucl. Energy* 120 (2020) 103220, <https://doi.org/10.1016/j.pnucene.2019.103220>.
- [45] M. Afiq, H. Abdullah, R. Saifulnaz, M. Rashid, M. Amran, F. Hejazii, N. Azreen, B. Masenwat, R. Fediuk, Y.L. Voo, N.I. Vatin, M.I. Idris, Recent trends in advanced radiation shielding concrete for construction of facilities: materials and properties, *Polymers* 14 (2022) 2830.
- [46] S. Mubarak, M. Muhammad Rashid, R.S. Amran, M. Fediuk, R. Vatin, N. Klyuev, Mechanical properties of high-performance hybrid fibre-reinforced concrete at elevated temperatures, *Sustainability* 13 (2021) 13392.
- [47] J. Du, W. Meng, K.H. Khayat, Y. Bao, P. Guo, Z. Lyu, A. Abu-obeidah, H. Nassif, H. Wang, New development of ultra-high-performance concrete (UHPC), *Compos. Part B Eng.* 224 (2021), <https://doi.org/10.1016/j.compositesb.2021.109220>.
- [48] M. Amran, G. Murali, N. Makul, W.C. Tang, A. Eid Alluqmani, Sustainable development of eco-friendly ultra-high performance concrete (UHPC): cost, carbon emission, and structural ductility, *Constr. Build. Mater.* 398 (2023), <https://doi.org/10.1016/j.conbuildmat.2023.132477>.
- [49] N.M. Azreen, R.S.M. Rashid, M. Haniza, Y.L. Voo, Y.H. Mugahed Amran, Radiation shielding of ultra-high-performance concrete with silica sand, amang and lead glass, *Constr. Build. Mater.* 172 (2018) 370–377, <https://doi.org/10.1016/j.conbuildmat.2018.03.243>.
- [50] V. Anish, J. Logeshwari, A review on ultra high-performance fibre-reinforced concrete with nanomaterials and its applications, *J. Eng. Appl. Sci.* 71 (2024), <https://doi.org/10.1186/s44147-023-00357-8>.
- [51] A. ASTM, C150/C150M-17, standard specification for Portland cement, Am. Soc. Test. Mater, West Conshohocken, PA, USA, 2017.
- [52] BS EN 12504-4, BS EN 12504. Testing concrete — Part 4: determination of ultrasonic pulse velocity, *Br. Stand. Inst.* 3 (2004) 18.
- [53] BS EN 12390-3:2019, BS EN 12390-3:2019 - Testing hardened concrete Compressive strength of test specimens, *Br. Stand. Inst.* (2019) 24.
- [54] D. Zhang, Y. Liu, K.H. Tan, Spalling resistance and mechanical properties of strain-hardening ultra-high performance concrete at elevated temperature, *Constr. Build. Mater.* 266 (2021), <https://doi.org/10.1016/j.conbuildmat.2020.120961>.
- [55] R. Yu, P. Spiesz, H.J.H. Brouwers, Mix design and properties assessment of Ultra-High Performance Fibre Reinforced Concrete (UHPFRC), *Cem. Concr. Res.* 56 (2014) 29–39, <https://doi.org/10.1016/j.cemconres.2013.11.002>.
- [56] A.M. Zeyad, I.Y. Hakeem, M. Amin, B.A. Tayeh, I.S. Agwa, Effect of aggregate and fibre types on ultra-high-performance concrete designed for radiation shielding, *J. Build. Eng.* 58 (2022) 104960, <https://doi.org/10.1016/j.job.2022.104960>.
- [57] E. Horszczaruk, P. Sikora, P. Zaporowski, Mechanical properties of shielding concrete with magnetite aggregate subjected to high temperature, *Procedia Eng.* (2015) 39–46, <https://doi.org/10.1016/j.proeng.2015.06.117>.
- [58] Y. Grosu, A. Faik, I. Ortega-Fernández, B. D'Aguanno, Natural Magnetite for thermal energy storage: Excellent thermophysical properties, reversible latent heat transition and controlled thermal conductivity, *Sol. Energy Mater. Sol. Cells* 161 (2017) 170–176, <https://doi.org/10.1016/j.solmat.2016.12.006>.
- [59] L.P.W. and J.E. Backstrom, Properties of Heavy Concrete Made with Barite Aggregates, *ACI J. Proc.* 51 (n.d.), <https://doi.org/10.14359/11668>.
- [60] H. Yao, I. Hatta, Phase transitions of quartz studied by a.c. calorimetry, *Thermochim. Acta* 266 (1995) 301–308, [https://doi.org/10.1016/0040-6031\(95\)02450-6](https://doi.org/10.1016/0040-6031(95)02450-6).
- [61] D. Levy, G. Artioli, M. Dapiaggi, The effect of oxidation and reduction on thermal expansion of magnetite from 298 to 1173 K at different vacuum conditions, *J. Solid State Chem.* 177 (2004) 1713–1716, <https://doi.org/10.1016/j.jssc.2003.12.032>.
- [62] S. Ismail Ahmed Ali, E. Lubløy, Effect of elevated temperature on the magnetite and quartz concrete at different W/C ratios as nuclear shielding concretes, *Nucl. Mater. Energy* 33 (2022), <https://doi.org/10.1016/j.nme.2022.101234>.
- [63] M. Amran, G. Murali, N. Makul, M. Kurpińska, M.L. Nehdi, Fire-induced spalling of ultra-high performance concrete: a systematic critical review, *Constr. Build. Mater.* 373 (2023), <https://doi.org/10.1016/j.conbuildmat.2023.130869>.
- [64] B. Li, T.C. Ling, J.G. Yu, J. Wu, W. Chen, Cement pastes modified with recycled glass and supplementary cementitious materials: properties at the ambient and high temperatures, *J. Clean. Prod.* 241 (2019), <https://doi.org/10.1016/j.jclepro.2019.118155>.
- [65] M.Z. Naser, V.A. Uppala, Properties and material models for construction materials post exposure to elevated temperatures, *Mech. Mater.* 142 (2020), <https://doi.org/10.1016/j.mechmat.2019.103293>.
- [66] A. Ergün, G. Kürklü, M. Serhat Başpınar, M.Y. Mansour, The effect of cement dosage on mechanical properties of concrete exposed to high temperatures, *Fire Saf. J.* 55 (2013) 160–167, <https://doi.org/10.1016/j.firesaf.2012.10.016>.
- [67] J.-F. Liang, Z.-P. Yang, P.-H. Yi, J.-B. Wang, Compressive behavior of recycled mortar after exposure to high temperatures, *Open Civ. Eng. J.* 10 (2016) 807–812, <https://doi.org/10.2174/1874149501610010807>.
- [68] Q.H. Li, C.J. Sun, S.L. Xu, Thermal and mechanical properties of ultrahigh toughness cementitious composite with hybrid PVA and steel fibers at elevated temperatures, *Compos. Part B Eng.* 176 (2019), <https://doi.org/10.1016/j.compositesb.2019.107201>.

- [69] W. Zheng, B. Luo, Y. Wang, Compressive and tensile properties of reactive powder concrete with steel fibres at elevated temperatures, *Constr. Build. Mater.* 41 (2013) 844–851, <https://doi.org/10.1016/j.conbuildmat.2012.12.066>.
- [70] E. Horszczaruk, P. Przozowski, Investigation of gamma ray shielding efficiency and physico-mechanical performances of heavyweight concrete subjected to high temperature, *Constr. Build. Mater.* 195 (2019) 574–582, <https://doi.org/10.1016/j.conbuildmat.2018.09.113>.
- [71] A. Behnood, M. Ghandehari, Comparison of compressive and splitting tensile strength of high-strength concrete with and without polypropylene fibers heated to high temperatures, *Fire Saf. J.* 44 (2009) 1015–1022, <https://doi.org/10.1016/j.firesaf.2009.07.001>.
- [72] W. Mahmood, T. Ayub, A. ur R. Khan, Mechanical properties and corrosion resistance of recycled aggregate concrete exposed to accelerated and natural marine environment, *J. Build. Eng.* 66 (2023), <https://doi.org/10.1016/j.jobe.2023.105867>.
- [73] L. Li, D. Gao, Z. Li, M. Cao, J. Gao, Z. Zhang, Effect of high temperature on morphologies of fibers and mechanical properties of multi-scale fiber reinforced cement-based composites, *Constr. Build. Mater.* 261 (2020), <https://doi.org/10.1016/j.conbuildmat.2020.120487>.
- [74] C.G. Han, Y.S. Hwang, S.H. Yang, N. Gowripalan, Performance of spalling resistance of high performance concrete with polypropylene fiber contents and lateral confinement, *Cem. Concr. Res.* 35 (2005) 1747–1753, <https://doi.org/10.1016/j.cemconres.2004.11.013>.
- [75] H. Wu, X. Lin, A. Zhou, Cement and Concrete Research A review of mechanical properties of fibre reinforced concrete at elevated temperatures, *Cem. Concr. Res.* 135 (2020) 106117, <https://doi.org/10.1016/j.cemconres.2020.106117>.
- [76] M. Hajsadeghi, M. Jalali, C. Seong Chin, T. Zirakian, M. Bahrebar, Flexural Characteristics of Fibre Reinforced Concrete with an Optimised Spirally Deformed Steel Fibre, *Int. J. Eng. Trans. A Basics* 34 (2021) 1390–1397, <https://doi.org/10.5829/ije.2021.34.06c.01>.
- [77] Y.S. Tai, H.H. Pan, Y.N. Kung, Mechanical properties of steel fibre reinforced reactive powder concrete following exposure to high temperature reaching 800 °C, *Nucl. Eng. Des.* 241 (2011) 2416–2424, <https://doi.org/10.1016/j.nucengdes.2011.04.008>.
- [78] G. Blasi, M. Leone, Inverse analysis-based model for the tensile behaviour of fibre-reinforced concrete with manufactured and waste tyres recovered fibres, *Case Stud. Constr. Mater.* 17 (2022), <https://doi.org/10.1016/j.cscm.2022.e01297>.
- [79] B. Georgali, P.E. Tsakiridis, Microstructure of fire-damaged concrete. A case study, *Cem. Concr. Compos.* 27 (2005) 255–259, <https://doi.org/10.1016/j.cemconcomp.2004.02.022>.
- [80] F.L. Bolina, G. Poletto, H. Carvalho, Proposition of parametric data for UHPC at high temperatures, *J. Build. Eng.* 76 (2023) 107222, <https://doi.org/10.1016/j.jobe.2023.107222>.
- [81] X. Huang, Z. Chen, Q. Tao, L. Xie, D. Jin, D. Wu, Effect of Magnetite Concrete on Splitting Tensile Strength and Gamma Ray Shielding Performance Exposed to Repeated Heating at High Temperature, *Mater. (Basel)* 16 (2023), <https://doi.org/10.3390/ma16072592>.
- [82] A. Mugahed, H. Shan-Shan, O.A.M. Murali, G. H.S. Abdelgader, Fire spalling behavior of high-strength concrete: A critical review, *Constr. Build. Mater.* 341 (2022) 127902.
- [83] V.K.R. Kodur, Spalling in high strength concrete exposed to fire - Concerns, causes, critical parameters and cures, : *Struct. Congr. 2000 Adv. Technol. Struct. Eng.* (2004), [https://doi.org/10.1061/40492\(2000\)180](https://doi.org/10.1061/40492(2000)180).
- [84] R.U.D. Nassar, O. Zaid, F. Althoej, M.A. Abuhussain, Y. Alashker, Spalling behavior and performance of ultra-high-performance concrete subjected to elevated temperature: a review, *Constr. Build. Mater.* 411 (2024), <https://doi.org/10.1016/j.conbuildmat.2023.134489>.
- [85] A.M. Zayed, M.A. Masoud, M.G. Shahien, H.S. Gökçe, K. Sakr, W.A. Kansouh, A.M. El-Khayatt, Physical, mechanical, and radiation attenuation properties of serpentine concrete containing boric acid, *Constr. Build. Mater.* 272 (2021), <https://doi.org/10.1016/j.conbuildmat.2020.121641>.
- [86] M.A. Masoud, A.M. El-Khayatt, W.A. Kansouh, K. Sakr, M.G. Shahien, A.M. Zayed, Insights into the effect of the mineralogical composition of serpentine aggregates on the radiation attenuation properties of their concretes, *Constr. Build. Mater.* 263 (2020), <https://doi.org/10.1016/j.conbuildmat.2020.120141>.
- [87] S.C. Kim, H.M. Jung, A study on performance of low-dose medical radiation shielding fiber (rsf) in ct scans, *Int. J. Technol.* 4 (2013) 178–187, <https://doi.org/10.14716/ijtech.v4i2.107>.
- [88] H. Mungpayaban, P. Rindhatayathon, S. Ninlaphruk, A. Rueanngoeng, S. Ekgasit, S. Pengprecha, X-ray protective materials from barium sulfate/amorphous cellulose/natural rubber composites, *Radiat. Phys. Chem.* 194 (2022) 110011, <https://doi.org/10.1016/j.radphyschem.2022.110011>.
- [89] S.J. Barnett, J.F. Lataste, T. Parry, S.G. Millard, M.N. Soutsos, Assessment of fibre orientation in ultra high performance fibre reinforced concrete and its effect on flexural strength, *Mater. Struct. Constr.* 43 (2010) 1009–1023, <https://doi.org/10.1617/s11527-009-9562-3>.
- [90] F. Köksal, F. Altun, I. Yiğit, Y. Şahin, Combined effect of silica fume and steel fiber on the mechanical properties of high strength concretes, *Constr. Build. Mater.* 22 (2008) 1874–1880, <https://doi.org/10.1016/j.conbuildmat.2007.04.017>.
- [91] A. Abrishambaf, J.A.O. Barros, V.M.C.F. Cunha, Relation between fibre distribution and post-cracking behaviour in steel fibre reinforced self-compacting concrete panels, *Cem. Concr. Res.* 51 (2013) 57–66, <https://doi.org/10.1016/j.cemconres.2013.04.009>.
- [92] C.S. Lu, J.X. Shen, P. Sun, Y. Poon, Strategy for preventing explosive spalling and enhancing material efficiency of lightweight ultra high-performance concrete, *Cem. Concr. Res.* 158 (2022) 106842.
- [93] E. Tajuelo Rodriguez, K. Garbev, D. Merz, L. Black, I.G. Richardson, Thermal stability of C-S-H phases and applicability of Richardson and Groves' and Richardson C-(A)-S-H(I) models to synthetic C-S-H, *Cem. Concr. Res.* 93 (2017) 45–56, <https://doi.org/10.1016/j.cemconres.2016.12.005>.
- [94] X. Hu, J. Xiao, Z. Zhang, C. Wang, C. Long, L. Dai, Effects of CCCW on properties of cement-based materials: a review, *J. Build. Eng.* 50 (2022), <https://doi.org/10.1016/j.jobe.2022.104184>.
- [95] M. Khan, J. Lao, M.R. Ahmad, J.G. Dai, Influence of high temperatures on the mechanical and microstructural properties of hybrid steel-basalt fibers based ultra-high-performance concrete (UHPC), *Constr. Build. Mater.* 411 (2024), <https://doi.org/10.1016/j.conbuildmat.2023.134387>.
- [96] S.T. Kang, J.I. Choi, K.T. Koh, K.S. Lee, B.Y. Lee, Hybrid effects of steel fiber and microfiber on the tensile behavior of ultra-high performance concrete, *Compos. Struct.* 145 (2016) 37–42, <https://doi.org/10.1016/j.compstruct.2016.02.075>.
- [97] M. Amran, S.S. Huang, A.M. Onaizi, N. Makul, H.S. Abdelgader, T. Ozbakkaloglu, Recent trends in ultra-high performance concrete (UHPC): Current status, challenges, and future prospects, *Constr. Build. Mater.* 352 (2022) 129029, <https://doi.org/10.1016/j.conbuildmat.2022.129029>.
- [98] R. Wang, X. Gao, J. Zhang, G. Han, Spatial distribution of steel fibers and air bubbles in UHPC cylinder determined by X-ray CT method, *Constr. Build. Mater.* 160 (2018) 39–47, <https://doi.org/10.1016/j.conbuildmat.2017.11.030>.
- [99] L. Shen, F. Lo Monte, G. Di Luzio, G. Cusatis, W. Li, R. Felicetti, F. Lombardi, M. Lualdi, M. Cao, Q. Ren, On the moisture migration of concrete subject to high temperature with different heating rates, *Cem. Concr. Res.* 146 (2021), <https://doi.org/10.1016/j.cemconres.2021.106492>.
- [100] G. Fang, M. Zhang, Multiscale micromechanical analysis of alkali-activated fly ash-slag paste, *Cem. Concr. Res.* 135 (2020), <https://doi.org/10.1016/j.cemconres.2020.106141>.
- [101] L. Sorelli, G. Constantinides, F.J. Ulm, F. Toutlemonde, The nano-mechanical signature of Ultra High Performance Concrete by statistical nanoindentation techniques, *Cem. Concr. Res.* 38 (2008) 1447–1456, <https://doi.org/10.1016/j.cemconres.2008.09.002>.
- [102] M. Chen, Z. Sun, W. Tu, X. Yan, M. Zhang, Behaviour of recycled tyre polymer fibre reinforced concrete at elevated temperatures, *Cem. Concr. Compos.* 124 (2021), <https://doi.org/10.1016/j.cemconcomp.2021.104257>.
- [103] S. Sanchayan, S.J. Foster, High temperature behaviour of hybrid steel-PVA fibre reinforced reactive powder concrete, *Mater. Struct. Constr.* 49 (2016) 769–782, <https://doi.org/10.1617/s11527-015-0537-2>.
- [104] Y. Li, K.H. Tan, E.H. Yang, Synergistic effects of hybrid polypropylene and steel fibers on explosive spalling prevention of ultra-high performance concrete at elevated temperature, *Cem. Concr. Compos.* 96 (2019) 174–181, <https://doi.org/10.1016/j.cemconcomp.2018.11.009>.
- [105] M. Zeiml, D. Leithner, R. Lackner, H.A. Mang, How do polypropylene fibers improve the spalling behavior of in-situ concrete? *Cem. Concr. Res.* 36 (2006) 929–942, <https://doi.org/10.1016/j.cemconres.2005.12.018>.